

Combined Fe-Mg chemical and isotopic zoning in olivine constraining magma mixing-to-eruption timescales for the continental arc volcano Irazú (Costa Rica) and Cr diffusion in olivine

MARTIN OESER^{1,*†}, PHILIPP RUPRECHT^{2,3}, AND STEFAN WEYER¹

¹Institut für Mineralogie, Leibniz Universität Hannover, Callinstrasse 3, 30167 Hannover, Germany

²Department of Geological Sciences, University of Nevada, 1664 N. Virginia Street, Reno, Nevada 89557, U.S.A.

³Lamont-Doherty Earth Observatory, Columbia University, 61 Route 9W, Palisades, New York 10964, U.S.A.

ABSTRACT

Arc magmas commonly are mixtures of newly arriving primitive melts, stored magmas at shallow levels, and xenolithic material added on ascent. Almost every eruption has a unique assembly of these components, which may record magmatic processes occurring in the plumbing system prior to an eruption. In this study, we focus on complexly zoned olivines (crustal xenocrysts) to obtain a better understanding of the magmatic processes and the assembly of the 1963–65 erupted magmas of Irazú volcano, one of the most voluminous active volcanoes in Costa Rica. We performed high-precision in situ Fe-Mg isotope analyses by femtosecond-LA-MC-ICP-MS on these olivines, to unravel the origin of their complex chemical zoning (growth, diffusion, or a combination of both processes). This information was used to establish a refined diffusion model to explore magma mixing-to-eruption timescales. Furthermore, trace element analyses using LA-ICP-MS were performed. Chromium displays a chemical zoning in the investigated olivine, which coincides spatially as well as in terms of length scale and geometry with Fe-Mg zoning and that was used to constrain Cr diffusivity in natural olivine.

Our findings show that Fe-Mg zoning in Irazú olivine mainly results from Fe-Mg inter-diffusion after two crystal growth episodes as indicated by strongly coupled chemical and isotopic zoning. Simulations of this diffusive process indicate that mixing of these crystals into ascending primitive melts occurred <600 days before their eruption, consistent with a previously reported diffusion study based on Ni zonation in Mg-rich olivines. Trace element characteristics of olivine suggest that the complex-zoned olivine crystals originate from a crystal mush/cumulate in the middle or lower crust and deeper than the shallow magma chamber and were mobilized by mantle-derived magma bearing Mg-rich olivines. Finally, modeling of the observed Cr zoning in the Irazú olivines indicates that the diffusion coefficient for Cr in olivine (D_{Cr}) is smaller than D_{Fe-Mg} by a factor of 4.9 ± 2.9 at the conditions experienced by these crystals consistent with Cr diffusion experiments at high silica activity in the melt.

Our results show that by combining elemental and isotope zoning studies in individual minerals we can refine the timing/assembly of magmatic eruptions and provide independent constraints on element diffusivities. Last, it confirms that primitive arc magmas at Irazú are not aphyric during ascent, but carry primitive phenocrysts from lower crust or Moho depth to the surface.

Keywords: Olivine, Fe-Mg zoning, stable isotopes, laser ablation, diffusion modeling, Cr diffusivity, magma assembly; Rates and Depths of Magma Ascent on Earth

INTRODUCTION

Intermediate arc magmas frequently contain diverse crystal populations, many of which are not in equilibrium with the host melt. As a result, many crystals re-equilibrate with their host melt either through chemical diffusion, crystallization/dissolution, or a combination of these processes. Snapshots of these transient processes, such as chemical zoning in crystals, are frozen at the time of eruption when magmas cool down rapidly. If diffusion is the dominant process to achieve equilibrium between crystal and melt, the chemical zoning can be used to obtain time information

about the evolution of magmatic systems by diffusion modeling, provided that diffusion rates of elements in the minerals of interest are known. The diffusion of Fe and Mg in olivine has been intensely investigated in experimental studies for more than 30 yr (reviewed by Chakraborty 2010), and several studies have used Fe-Mg chemical gradients in magmatic olivine crystals to estimate timescales of magma evolution processes by diffusion modeling (e.g., Costa and Chakraborty 2004; Costa and Dungan 2005; Kahl et al. 2011, 2013; Hartley et al. 2016; Rae et al. 2016), relying on the parameterization for the Fe-Mg inter-diffusion coefficient given by Chakraborty (1997) and Dohmen and Chakraborty (2007). However, as crystal growth and elemental diffusion often show similar zoning patterns it remains questionable whether calculated diffusion timescales represent the timing of a specific magmatic process (Shea et al. 2015).

*E-mail: m.oeser@mineralogie.uni-hannover.de

† Special collection papers can be found online at <http://www.minsocam.org/MSA/AmMin/special-collections.html>.

As shown in recent studies, combining the information of Fe-Mg chemical variations and in situ analyses of Fe-Mg stable isotope ratios in olivine represents a powerful means to elucidate diffusion and/or growth/dissolution processes (Sio et al. 2013; Oeser et al. 2015). As diffusion generates large kinetic isotope fractionations (e.g., Richter et al. 2003) diffusion-generated chemical zoning is coupled with pronounced isotopic zoning, in contrast to chemical zoning that developed in absence of diffusion (Oeser et al. 2015). Detailed chemical and isotopic profiles across magmatic olivines may thus be used to unravel complex crystal growth- and diffusion histories, which are indistinctly recorded by chemical zoning alone (e.g., Collinet et al. 2017; Sio and Dauphas 2017).

In this study, we aim to investigate the magmatic events recorded in complexly zoned olivine crystals in basaltic andesites of the 1963–65 eruption of the Irazú volcano, one of the most voluminous (e.g., Carr 1984) and active volcanoes in Costa Rica, with recurring explosive andesitic eruptions potentially endangering ~1.6 million people living within 30 km of this stratovolcano (Global Volcanism Program 2013). Previously, investigation of Ni zoning in primitive (magnesian) olivines from this eruption suggested that magma transport from the Moho to the surface occurred on timescales comparable to the duration of the eruption (~2 yr), thus indicating that the eruption was likely fed (and triggered) by magmas extracted from the mantle (Ruprecht and Plank 2013). This study provides a more comprehensive picture of the pre-eruptive mixing and assembling of erupted 1963–65 magmas, focusing on complexly zoned (in terms of Fo contents) olivines. These crystals share the normal zoning history of the rims of the mantle-derived magnesian olivines. By unraveling the origin of their complex zoning, we establish the basis for appropriate diffusion modeling. This will eventually yield reliable mixing-to-eruption timescales and provide a more detailed picture of the complex history of these crystals, leading to a better understanding of the magmatic processes and the assembly of the erupted magmas beneath Irazú volcano.

Moreover, through the refinement of timescale estimates using in situ isotope records we can also assess the diffusivity of slow-diffusing elements, for which experimental studies are challenging (e.g., Milman-Barris et al. 2008). Natural samples have been used elsewhere (e.g., Mallmann et al. 2009; Qian et al. 2010; Tollar et al. 2015) to compare results to experimentally determined diffusion coefficients (e.g., Ito and Ganguly 2006; Spandler and O'Neill 2010; Zhukova et al. 2017; Jollands et al. 2014, 2018). Notably, Cr diffusivities display a large range in the literature (Ito and Ganguly 2006; Milman-Barris et al. 2008; Spandler and O'Neill 2010; Jollands et al. 2018). The recent study of Jollands et al. (2018) suggested that this large range is a result of variations in SiO_2 activity (a_{SiO_2}), an effect that has also been recognized for other trace elements in olivine (Jollands et al. 2014, 2016a; Zhukova et al. 2014). Independent timescale estimates (specifically more robust by combining elemental and isotopic zoning) can also be used to constrain diffusivities of such slow-diffusing elements and help to provide additional constraints to reconcile variations in experimentally determined diffusivities. The complexly zoned olivine crystals in basalts of the 1963–65 eruption that are close to the SiO_2 activity buffer of olivine-enstatite are suitable for such an approach since Fe-Mg zoning coincides with Cr zoning (and to a lesser extent also V and Al zoning).

THE IRAZÚ MAGMA SYSTEM AND SAMPLES

The Irazú magmatic plumbing system has been characterized geophysically and geochemically (Alvarado et al. 2006; Dzierma et al. 2010; Ruprecht and Plank 2013). Seismic studies highlight a low-velocity region in the upper crust (5–10 km) commonly interpreted to represent the major magma storage region. Furthermore, the Moho depth has been constrained seismically to ~35–45 km (Lizarralde et al. 2010; Gazel et al. 2015).

Geochemical constraints emphasize the hybrid nature of Irazú magmas, particularly the 1963–65 eruption (Alvarado et al. 2006). Whole-rock compositions represent mixtures of basaltic and dacitic end-members. While geophysics and whole-rock geochemistry provide a simplified view of the magma plumbing system, more detail is recorded within the crystal cargo. First, crystals from individual samples show a large compositional diversity that mimics the whole rock end-members (An_{40-80} , Fo_{72-91} ; Alvarado et al. 2006; Ruprecht and Plank 2013). However, a detailed look into the crystal cargo reveals that it is inadequate to explain the complex crystal cargo with mantle-derived magmas that simply rise to the shallow region where they differentiate and hybridize. In this study we focus on olivine crystals (with xenocrystic cores; see below) that provide a unique view into the magma assembly from the mantle to the surface. Ruprecht and Plank (2013) reported on the major and trace element geochemical diversity in olivines from the 1963–65 eruption. Based on their results, at least three different olivine types in the Irazú eruption can be distinguished: (1) magnesian olivines (Fo_{89-91}) that were the focus of Ruprecht and Plank (2013, type A); (2) complex olivines that show significant reversals in their Fo contents and are the focus of this study (type B); and (3) intermediate- to low-Fo olivines at low-Ni content that represent shallow crustal processes of fractionation and mixing (type C; Fig. 1). It is notable here that these three types of olivines represent end-member compositions, and the full olivine population shows crystals that are intermediate between those end-members. Potentially, the “reservoirs” that are represented by the three olivine end-members have either some internal variation, e.g., due to incomplete mixing (Ruprecht et al. 2008; Schleicher and Bergantz 2017) resulting in a range in composition, or they are partially open to interact with each other beyond just the processes directly driving the 1963–65 eruption. In the “Results” section we are going to describe in greater detail the type B olivines, which are the main focus of this study. The samples analyzed herein (IZ-10-11/-12/-13) comprise crater rim deposits of the 1963–65 eruption on the southwest side of the major Irazú crater, which are juvenile scoria-rich tephra and fine lapilli tephra (Ruprecht and Plank 2013). From these samples, we investigated 10 olivine crystals (three of type A, seven of type B) for their major and trace elements characteristics and their Fe- and Mg-isotopic compositions by microanalytical techniques (see next section).

METHODS

In situ major and trace element analyses of olivines

Major and trace element laser ablation data were analyzed using a VG PQ ExCell and NewWave 196 nm ArF Eximer laser at Lamont-Doherty Earth Observatory during the study of Ruprecht and Plank (2013). The data acquisition was done in line mode and the continuous time series data was then processed into individual data points by combining a finite number of steps. Each sweep from Li-7 to Y-89 took 0.36 s, with dwell times of 10 ms on each mass (for all masses analyzed see

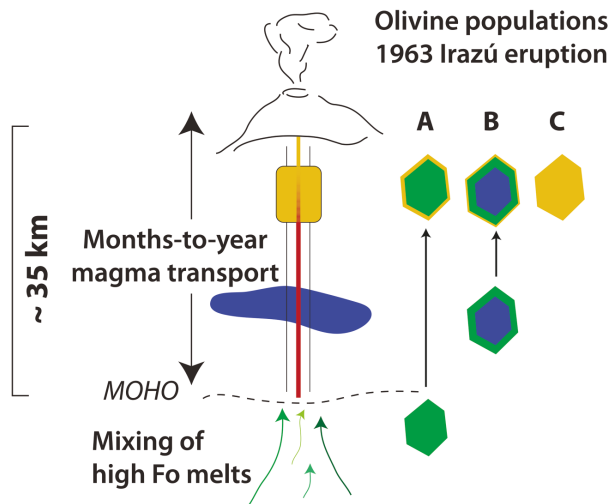


FIGURE 1. Schematic architecture of Irazú magma system (modified from Ruprecht and Plank 2013) and the origin of distinct olivine types A–C. Green represents primitive magnesian olivines (Fo_{89-91}), or the Mg-rich rims (Fo_{87-90}) grown around crystal cores with intermediate-Fo contents (Fo_{80-87} , blue) when the latter were picked up by ascending mantle melts. Orange represents normally zoned (Fo_{87-90} to Fo_{79-84}) outer rims of olivine crystals or intermediate- to low-Fo olivines from the shallow magma storage region. (Color online.)

Supplemental¹ Table S1). The raw data was processed following standard calibration techniques for LA-ICP-MS (using a Matlab code developed by P. Ruprecht), but using Fe and Mg count rates and olivine stoichiometry to calculate the internal standard concentration of MgO. Comparisons with microprobe profiles show that for magnesian olivines this procedure produces Fo contents within 0.5 mol units of electron microprobe results (Ruprecht and Plank 2013). San Carlos olivine USNM 1113142/44 was used to normalize results from different days and to assess the measurement uncertainties. While this procedure may introduce a small systematic difference to other data sets in the literature related to potentially small heterogeneities in San Carlos trace element abundances across labs, it ensures that analyses are internally comparable. The concentrations used for San Carlos olivine were reported in Ruprecht and Plank (2013) and recalculation to other standards is trivial. A more detailed San Carlos olivine study is underway, but it is not the scope of this paper. The combined data points are recorded for every 5.8 μm , which is less than the spot size of the laser (25 μm) and therefore does not represent the true spatial resolution of the analysis. Given the continuous movement across the sample (3 $\mu\text{m/s}$), some smearing of the signal will occur and the spatial resolution is therefore similar to the laser spot size (Bradshaw and Kent 2017). Recently we recognized that in our instrument Ca concentration data are affected by interference of ^{28}Si and ^{16}O on mass 44, thus the Ca data needs to be interpreted cautiously. We focus here on inferred Fo content as well as the cations V, Cr, and Al. Al counts were statistically indistinguishable from the background for one sample (IZ-10-13), which was measured on a different day than IZ-10-12, which was measured during a day of better instrument sensitivity. LA-ICP-MS results of the olivines investigated in this study can be found in the supplementary¹ material (Table¹ S1). Olivines were repolished after these LA-ICP-MS analyses to determine crystal orientations by electron backscatter diffraction (see below) and to acquire BSE images.

In situ Fe and Mg isotope analyses of zoned olivines

Profiles of Fe and Mg isotopic compositions in zoned olivines were acquired in situ by femtosecond-laser ablation-MC-ICP-MS (fs-LA-MC-ICP-MS) at the Institut für Mineralogie of the Leibniz Universität Hannover, following the analytical procedures described in Oeser et al. (2014, 2015). In summary, a Spectra-Physics Solstice fs-LA system is coupled to a Thermo-Finnigan Neptune Plus MC-ICP-MS, which is operated in high mass resolution mode to resolve molecular interferences of argon nitrides and argon oxides on Fe isotopes and isobaric interferences (e.g., $^{52}\text{Cr}^{2+}$) on Mg isotopes. Laser repetition rate was between 30 and 70 Hz during Fe isotope analyses and between 20 and 45 Hz during Mg isotope analyses, depend-

ing on the Fe and Mg concentrations in the ablated material. Fluence of the fs-LA system in Hannover is on the order of 1 J/cm². Further details of the fs-LA system can be found in Oeser et al. (2014) and Lazarov and Horn (2015). The instrumental mass discrimination of the MC-ICP-MS was monitored during Fe isotope ratio determination by simultaneously analyzing the Ni isotope ratios of a Ni reference solution (NIST SRM 986) combined with a sample-standard bracketing protocol. For Mg isotope analyses, only the sample-standard bracketing technique was used to correct for drifts of the instrumental mass bias. With this analytical procedure, the LA analyses yield a long-term reproducibility of $\pm 0.13\text{\textperthousand}$ (2 SD) for both $\delta^{56}\text{Fe}$ and $\delta^{26}\text{Mg}$, based on replicate analyses of silicate reference glasses (e.g., BHVO-2G, ML3B-G) over a period of three years. During a single analytical session (1–2 days) the reproducibility of $\delta^{56}\text{Fe}$ and $\delta^{26}\text{Mg}$ values for the reference glasses is always better than $\pm 0.10\text{\textperthousand}$ (2 SD). The LA analyses on olivines from Irazú were guided by previously acquired BSE images (Ruprecht and Plank 2013). Sample material was ablated with a laser spot size of 35–40 μm (in diameter) by line scans either (1) parallel to the crystal rim (i.e., parallel to the chemical zoning; Figs. 2a and 2b) with a laser scan speed of 20 $\mu\text{m/s}$ and a cycle integration time of ~ 1 s or (2) perpendicular to it with a laser scan speed of 2–3 $\mu\text{m/s}$ and a cycle integration time of ~ 0.5 s (Figs. 2c and 2d). The latter technique was applied if the exposed area on the crystal was not sufficient to perform line scans (with sizes of $\sim 150 \times 40$ μm) parallel to the chemical zoning. In case 1, one ablation line yields one δ -value. In case 2, the mean of 15–20 individual ratio measurements is used to calculate one δ -value. As a consequence, the precision (2σ) of a single δ -value determined in such a way is usually not as high as for case 1, i.e., better than $\pm 0.10\text{\textperthousand}$, but still better than the long-term reproducibility of $\pm 0.13\text{\textperthousand}$. For case 2, 2σ is calculated by propagating the errors (SE) of the bracketing standards ($n \approx 120$ cycles) and of the analyzed sample ($n = 15–20$ cycles), as follows:

$$2\sigma = 2 \times 1000 \times \left[\left(\frac{SE_{\text{std1}}}{R_{\text{std1}}} \right)^2 + \left(\frac{SE_{\text{std2}}}{R_{\text{std2}}} \right)^2 + \left(\frac{SE_{\text{sample}}}{R_{\text{sample}}} \right)^2 \right]^{0.5} \quad (1)$$

where R is either $^{56}\text{Fe}^{/54}\text{Fe}$ or $^{26}\text{Mg}^{/24}\text{Mg}$.

Electron microprobe and electron-backscattered diffraction analyses

After the in situ isotope ratio analyses by fs-LA-MC-ICP-MS, all olivine crystals were carefully repolished, thus removing a layer of ~ 10 μm in thickness. Because the laser ablation lines have approximately a Gaussian shape (in cross section; Supplemental¹ Figs. S1 and S2), this repolishing decreased the sizes of the LA lines significantly, enabling us to determine major and minor element concentrations by electron microprobe analyses (EMPA) very close to the isotopic profiles.

A Cameca SX-100 with 5 wavelength-dispersive spectrometers at the American Museum of Natural History in New York was used for post-isotope analysis electron microprobe work. Analyses were performed utilizing a focused beam (1 μm diameter), 20 nA beam current, and 15 kV accelerating voltage. The instrument was calibrated on forsterite [Mg (30 s, peak counting times), TAP (analyzer crystal)], plagioclase [Al (60 s), TAP], clinopyroxene [Si (30 s), TAP; Ca (80 s), PET], magnesiocromite [Cr (40 s), LPET], rhodonite [Mn (40 s), LPET], fayalite [Fe (30 s), LLIF], and Ni-diopside [Ni (60 s), LLIF]. Reference olivines San Carlos and Ol174.1 ($n = 5$ each) were measured together with unknowns. We estimate the reproducibility from the repeat measurements of reference olivines to be within $\sim 2\%$ (2 SD relative), $<5\%$, $<20\%$, and $<50\%$ for major elements, Ni, Mn, and Ca, respectively. Calculated Mg# for San Carlos (89.79 ± 0.09 , 2 SD absolute) and Ol174.1 (90.24 ± 0.33) are within error of published values (White 1966; Jarosewich et al. 1980). Cr and Al in reference materials were below the detection limits for this analytical protocol (~ 200 ppm), but analyzed to identify mixed analyses with spinel. A complete table of quantitative electron microprobe analyses together with BSE images can be found in Supplemental¹ Table S2.

To account for diffusive anisotropy crystal lattice orientations relative to the 1D-zoning traverses were determined via electron-backscattered diffraction (EBSD). EBSD measurements were performed as part of the analytical session reported in Ruprecht and Plank (2013). A Zeiss Supra 40VP scanning electron microscope, Oxford energy-dispersive X-ray spectroscopy and HKL electron backscatter diffraction (EBSD) integrated system was used at the Marine Biological Laboratory in Woods Hole. Diffraction patterns were matched against a reference olivine lattice model and Euler angles were recorded for a rotation from the reference frame to the observed orientation. Rotation information is provided in Supplemental¹ Table S3.

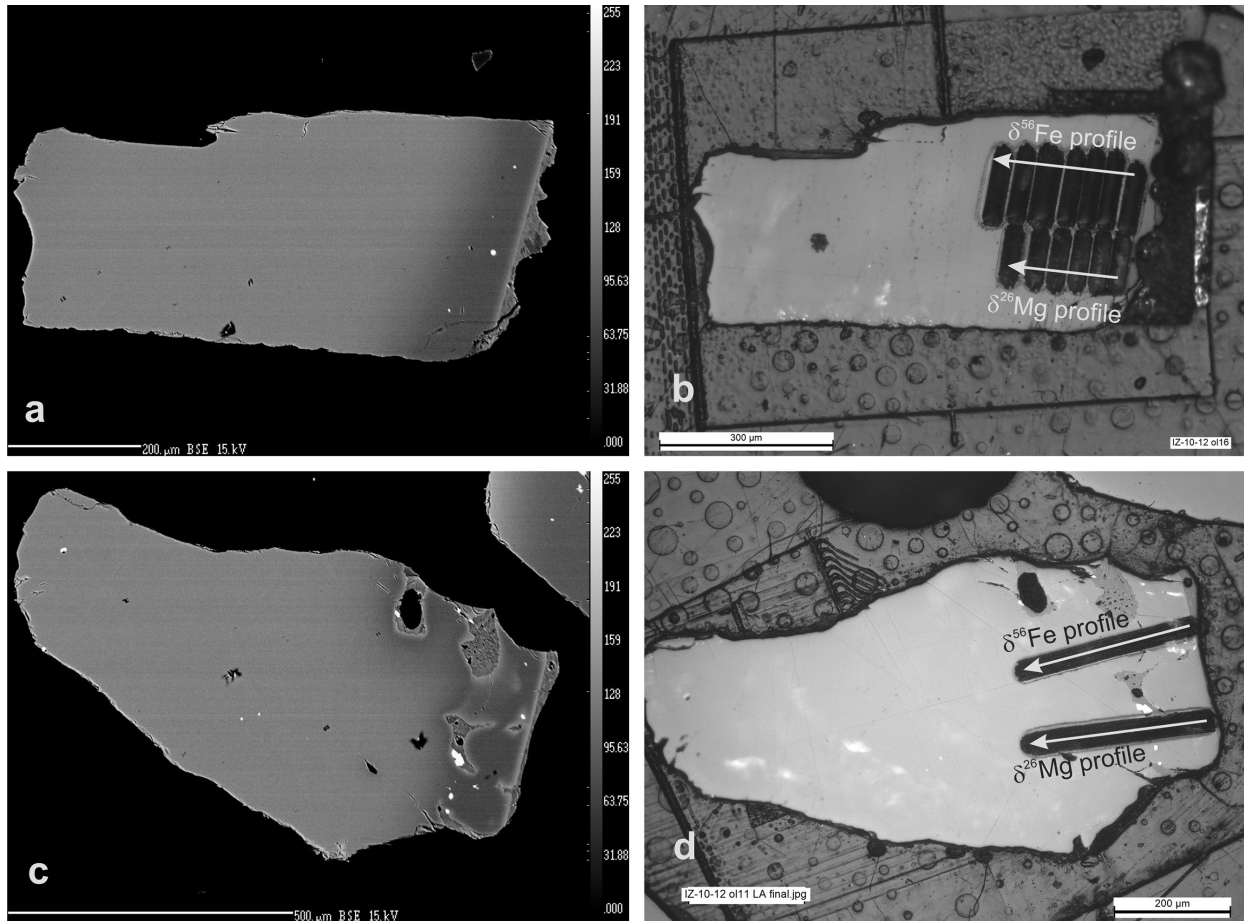


FIGURE 2. BSE and reflected-light images of two olivine crystals investigated in this study. (a and c) BSE images of crystals IZ-10-12 ol11 and IZ-10-12 ol11, respectively, before in situ analyses of Fe-Mg isotopic profiles by LA-MC-ICP-MS. (b and d) Reflected-light images of the same crystals after the in situ analyses by LA-MC-ICP-MS.

RESULTS

As described above, the Irazú 1963–65 samples investigated by Ruprecht and Plank (2013) and in this study contain principally three different olivine types. We define type B olivines as large crystals ($>500 \mu\text{m}$) with intermediate-Fo core (Fo_{80-87}). Reverse zoning from the core to the mantle of the crystals links the crystallization history of type A and type B olivines (Fig. 1). The high-Fo mantles never reach the most magnesian compositions recorded in type A olivines, but join the normal zonation near the rim at $\sim\text{Fo}_{87}$ to $\text{Fo}_{90.5}$. The mantle zoning of major elements in type A and B is correlated with the same zoning features in minor and trace elements (e.g., Ni, Cr, Al, V; Fig. 3). In contrast, the cores of these two types are significantly different also in trace element inventory (Fig. 4). Exemplary for this difference are the elevated Ni and low Cr concentrations, a trace element signature that is consistent with a xenocrystic origin for the type B cores. Such signatures are commonly associated with olivine cumulates (e.g., Otamendi et al. 2016), where partitioning and diffusive exchange of Ni and Cr leads to a preferential incorporation in olivine and pyroxenes, respectively.

Given the zoning characteristics of the different olivines in the 1963–65 eruption, exploring their relative contributions to

individual samples shows that the crystal cargo changed as the eruption progressed. We have only investigated three samples (IZ-10-11/12/13) that represent early, middle, and late stages of the eruption (see Ruprecht and Plank 2013, for the sampling levels and further sample details). Some coexisting lavas also were investigated petrographically (samples from Benjamin et al. 2007), but have not been investigated as detailed as the tephra samples. While all samples contain type A and type C olivines at fractions in significant quantities, type B olivines are rare in the early sample (IZ-10-11).

More specifically, the seven complexly zoned olivine crystals from Irazú volcano investigated in this study show reversely zoned ferrous cores (Fo_{80-87} to Fo_{87-90} , Fig. 5, Supplemental¹ Fig. S3), likely indicating (at least) two episodes of crystal growth. The rims of these crystals are always normally zoned (Fo_{87-90} to Fo_{79-84} , Fig. 5). Hence, as mentioned above, they appear to share the history of the rims of primitive magnesian olivines in the samples of the 1963–65 eruption of Irazú volcano. This normal chemical zoning at the rims may indicate either (1) crystal growth during fractional crystallization of olivine and clinopyroxene (and thus an evolution of the melt to higher Fe-Mg ratios) or (2) diffusion of Fe into and Mg out of olivine driven by a com-

positional contrast between olivine and melt or (3) a combination of both processes. As shown in previous studies, Fe-Mg isotopic profiles in such chemically zoned olivines can unravel which of the three possibilities is the most likely one (Sio et al. 2013; Oeser et al. 2015; Richter et al. 2016; Sio and Dauphas 2017). Other means to distinguish between growth- and diffusion-generated zoning in a crystal include, for example, the investigation (1) of zoning profile lengths of various elements with different known diffusivities (e.g., Costa and Dungan 2005), and (2) of the width of the chemical zoning in different crystallographic directions expected from diffusion anisotropy (e.g., Costa et al. 2008).

Three solely normally zoned (Mg-rich) olivine crystals investigated in this study show more or less homogeneous cores (Fo_{88-90}) and strongly zoned rims (Fo_{88} to Fo_{78-80} , Fig. 6). One of these olivines (IZ-10-13 ol22) additionally shows reverse Ni zoning in its core, which has already been investigated by Ruprecht and Plank (2013).

Our in situ Fe-Mg isotope data reveal a strong coupling of Fe-Mg chemical and isotopic zoning for all investigated olivines (Figs. 5 and 6, Supplemental¹ Fig. S3), along with largely

negative correlations between $\delta^{26}\text{Mg}$ and $\delta^{56}\text{Fe}$ values (Fig. 7), indicating that Fe-Mg inter-diffusion is the dominant process responsible for the re-equilibration of these olivines (cf. Teng et al. 2011; Sio et al. 2013; Oeser et al. 2015). A few Mg isotope data points clearly deviate from the overall negative correlations between $\delta^{26}\text{Mg}$ and $\delta^{56}\text{Fe}$ values (Fig. 7). The origin of these “outliers” is unknown, but may be related to the fact that Mg and Fe isotope profiles for a certain olivine cannot be measured at the exact same positions in the crystal (see Fig. 2). Nevertheless, in these relatively Mg-rich olivines (Fo contents vary between 78 and 90 mol%), Fe isotope variations are much more pronounced than Mg isotope variations (Fig. 7), for mass-balance reasons, and thus can put tighter constraints on the history of these crystals (see section “Discussion”). As a consequence, we will focus on Fe isotopic zoning, in combination with Fe-Mg chemical zoning, in the following sections. However, in the supplementary material we also show modeling results for Mg isotopic zoning in some olivine crystals (Supplemental¹ Fig. S4).

The olivines investigated here for Fe-Mg isotopes have a distinct trace element characteristic. In particular, the olivines

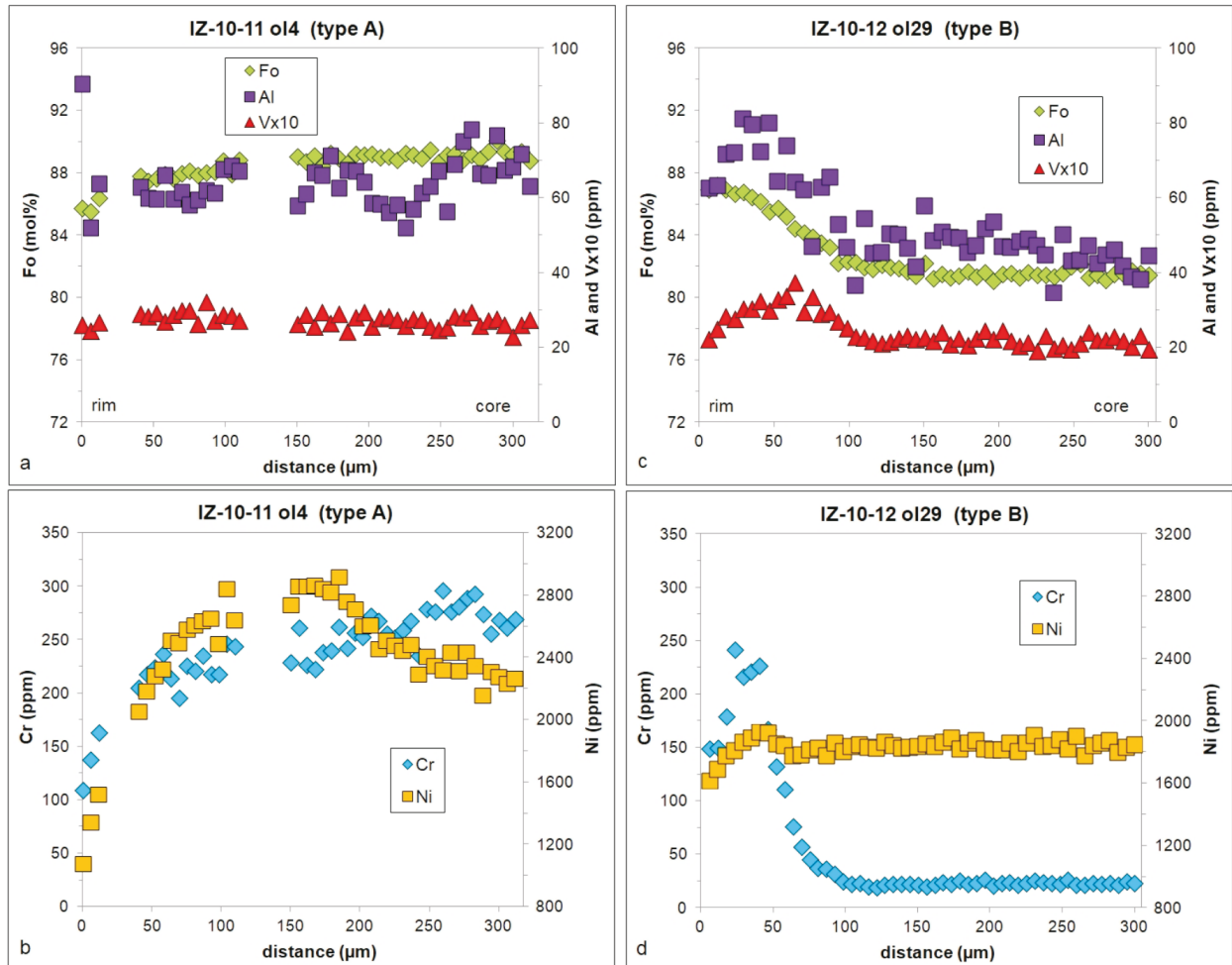


FIGURE 3. Examples of type A (a and b) and type B (c and d) olivine crystals from Irazú. Type A olivines show reverse Ni zoning at constant and high Fo and Cr contents in their cores, while type B olivines display reverse zoning of Fo and Cr (and in some cases also of Al and V) as well as very low Cr concentrations in their cores. (Color online.)

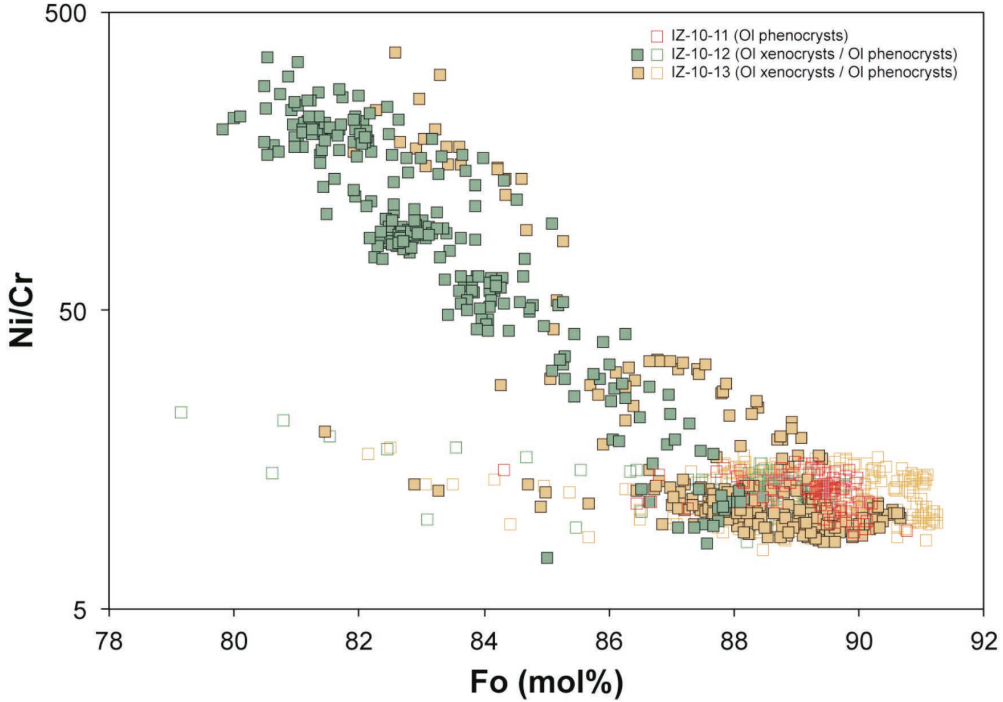


FIGURE 4. Ni/Cr vs. Fo content in olivines investigated in this study. Type B olivines are characterized by large Ni/Cr ratios, while type A olivines are constrained to low Ni/Cr ratios at high-Fo content. All core-to-rim data for Type B crystals are labeled as xenocrysts and therefore xenocryst rims plot at low Ni/Cr ratios. (Color online.)

with intermediate-Fo, high-Ni cores overgrown by high-Fo, high-Ni rims have unique Cr concentrations among all 1963–65 Irazú olivines. The cores have low-Cr concentrations in a few crystals less than 10 ppm (Fig. 3), which is uncommon for primitive magmatic olivine phenocrysts, and stands in contrast to the high-Ni content for the given Fo content. On the other hand, the high-Fo rims have Cr contents that are more common in primitive arc olivines >100 ppm. This extreme difference between those cores and the rims and any other primitive Irazú olivine is best expressed in the Ni/Cr ratio, which for normal olivines ranges between 10 and 15, but reaches 370 in some cores of the intermediate-Fo, high-Ni olivines (Fig. 4).

In addition to the unique Ni/Cr ratios, the zoning of trace elements generally correlates with major element zoning and therefore can potentially be linked to the timescales obtained here via the Fe-Mg isotopes and Fe-Mg elemental zoning. We note that many trace elements have zoning that correlates with major element zoning, however, we focus here solely on Cr, V, and Al zoning, because these have received particular attention given the recent controversy about their diffusivities in olivine (Ito and Ganguly 2006; Spandler et al. 2007; Milman-Barris et al. 2008; Spandler and O'Neill 2010). For all crystals that have zoning of Cr, V, and Al, the length scales of the zoning are shorter than the Fe-Mg zoning, however of a similar order of magnitude.

Diffusion modeling

The simulation of observed Fe-Mg chemical and isotopic zoning in Irazú olivines by diffusion modeling generally follows the approaches presented in Oeser et al. (2015). In particular, to

reproduce the reverse zoning of the complexly zoned olivines (hereafter referred to as diffusion episode 1) two models were applied: the first one comprises the internal homogenization of an olivine by Fe-Mg inter-diffusion after two growth episodes that generate a step function in the Fo content profile (magnesian rim, ferrous core) but homogeneous Fe and Mg isotopic compositions (scenario 3 in Oeser et al. 2015). For this case, we assumed a plane sheet geometry and solved the following one-dimensional expression of the diffusion equation numerically by the method of finite differences (e.g., Crank 1975; Costa et al. 2008):

$$\frac{\partial C_i(x,t)}{\partial t} = \frac{\partial}{\partial x} \left[D_i \frac{\partial C_i(x,t)}{\partial x} \right] \quad (2)$$

where C_i is the concentration of element i , t is time, D_i is the diffusion coefficient of element i , and x is distance. The second possible model encompasses the growth of a Mg-rich rim around a homogeneous ferrous olivine crystal, but now associated with simultaneous Fe-Mg inter-diffusion (scenario 4 in Oeser et al. 2015). Here, the olivine is assumed to be a semi-infinite medium, and we use the same analytical solution to this moving boundary problem as given in Oeser et al. (2015):

$$c(x,t) = C_0 + (C_{\text{rim}} - C_0) \times \exp \left[\frac{R \left(x - \frac{Rt}{2} \right)}{2D} \right] \frac{1}{2} \exp(\lambda t) \\ \left\{ \exp \left(-x \sqrt{\frac{\lambda}{D}} \right) \text{erfc} \left[\frac{x}{2\sqrt{Dt}} - \sqrt{\lambda t} \right] + \exp \left(x \sqrt{\frac{\lambda}{D}} \right) \text{erfc} \left[\frac{x}{2\sqrt{Dt}} + \sqrt{\lambda t} \right] \right\} \quad (3)$$

where C_0 is the initial concentration of the element of interest (as measured in the core of the olivine crystal), C_{rim} is the concentration of this element in the overgrowing rim, t is time, D is the diffusion coefficient, R is the growth rate, $\lambda = R^2/(4D)$, and x is distance.

Simple Fe-Mg exchange between olivine and melt (scenario 1 in Oeser et al. 2015) was modeled by applying a fixed rim composition and Fe-Mg inter-diffusion in olivine with a plane sheet geometry. In this case, the diffusion equation (Eq. 2) was solved numerically by the method of finite differences. This model was used to reproduce the normal zoning at the rims of the investigated olivines from Irazú volcano (hereafter referred to as diffusion episode 2). Further initial and boundary conditions are given in the following paragraph and in section “Diffusion episode 1.”

According to the parameterization given by Dohmen and Chakraborty (2007), which we applied in this study, the diffusion coefficient for Fe-Mg diffusion in olivine depends on oxygen fugacity (f_{O_2}), the mole fraction of the fayalite component (X_{Fe}), pressure (P), temperature (T), and the crystallographic orientation, i.e., the orientation of each measured profile relative to the crystallographic axes determined by electron backscatter diffraction. The latter was used to calculate the diffusion coefficient for

individual profiles, following the approach given in, e.g., Costa and Chakraborty (2004). The presence of water in an olivine crystal can also significantly affect $D_{\text{Fe-Mg}}$ in olivine (Wang et al. 2004; Hier-Majumder et al. 2005). We have not investigated whether the Irazú olivines contain significant amounts of water (i.e., >11 ppm, as reviewed by Chakraborty 2010), and thus we do not account for effects from hydrogen. However, Irazú magmas commonly contain ~3 wt% H_2O (Benjamin et al. 2007) and coexisting olivines may contain therefore significant amounts of water. Thus, our modeled timescales represent maximum estimates, as the presence of H^+ in olivine increases $D_{\text{Fe-Mg}}$ by up to one order of magnitude relative to anhydrous conditions (e.g., Jollands et al. 2016b). The durations of the diffusive processes were estimated at isothermal conditions, and temperature estimations in this study rely on thermometry data for Irazú magmas presented in Alvarado et al. (2006), Benjamin et al. (2007), and Ruprecht and Plank (2013). In particular, for diffusion episode 1 we assumed a temperature of 1150 °C, consistent with the temperature range (1100–1200 °C) used for simulating Ni diffusion profiles in the magnesian olivines from Irazú (Ruprecht and Plank 2013). For the second diffusion episode, a temperature of 1080 °C was used for diffusion modeling, consistent with

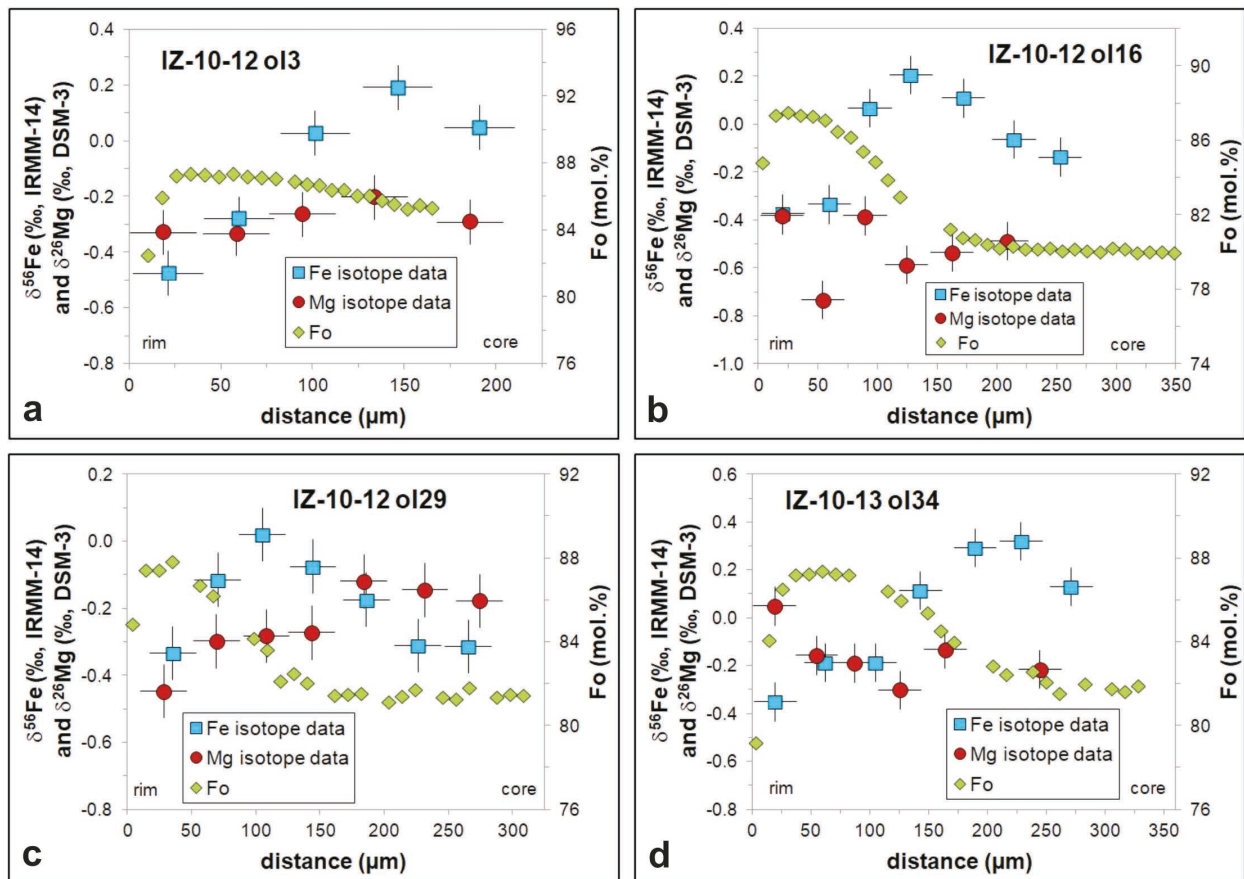


FIGURE 5. Fe-Mg chemical (expressed as Fo) and isotopic profiles for four complexly zoned olivines analyzed in this study. All olivines show strong coupling of Fe-Mg chemical and isotopic zoning (especially for Fe isotopes), indicating equilibration by Fe-Mg inter-diffusion. Sample material of these four olivine crystals was ablated by line scans parallel to the chemical zoning. Error bars represent the analytical uncertainty (2 SD) during one analytical session. (Color online.)

temperature estimations based on whole rocks and melt inclusions of more evolved compositions (Benjamin et al. 2007), as this diffusion event likely occurred in the plumbing system in the shallow crust (see below). The oxygen fugacity was assumed to be $\Delta \log f_{\text{O}_2}$ (NNO) = +1 (Benjamin et al. 2007), and its absolute value at the given temperature was calculated following

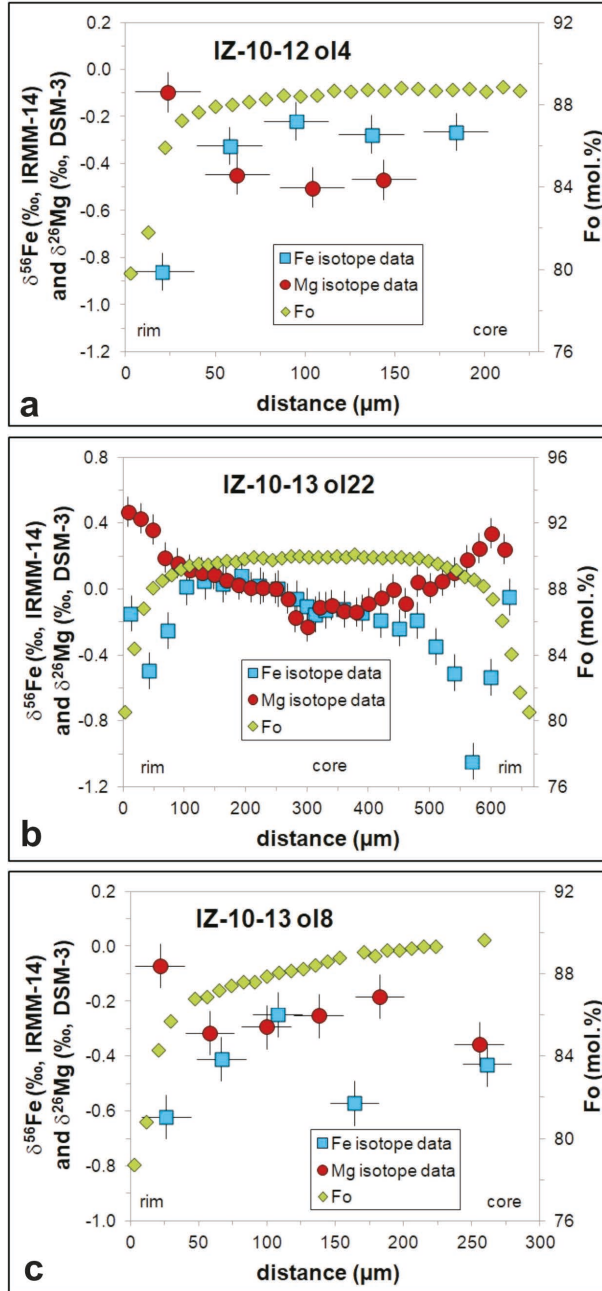


FIGURE 6. Fe-Mg chemical (expressed as Fo) and isotopic profiles for three primitive, normally zoned olivines investigated in this study. The normal zoning at the rim is strongly coupled with inversely correlated Fe-Mg isotopic profiles, implying diffusive re-equilibration prior to eruption. Sample material of olivine IZ-10-13 ol22 was ablated by line scans perpendicular to the chemical zoning. Error bars represent the analytical uncertainty (2 SD) during one analytical session. (Color online.)

the parameterization of Schwab and Küstner (1981). As the compositional variability concerning X_{Fe} is limited, i.e., fayalite contents range from 0.22 to 0.12 for the investigated olivines, X_{Fe} was presumed to be constant at an average value of 0.15 in all simulations. The uncertainty introduced by this simplification on $D_{\text{Fe-Mg}}$ (and, hence, on the calculated timescales) is smaller than a factor of 1.6. Pressure variations have the least effect on $D_{\text{Fe-Mg}}$, compared to variations in $T, f_{\text{O}_2}, X_{\text{Fe}}$, or orientation, and given the pressure range experienced by the investigated olivine crystals (~0.1–500 MPa). Following the pressure estimation made for the magnesian Irazú olivines (Ruprecht and Plank 2013) we assumed P to be 500 and 100 MPa during diffusion episodes 1 and 2, respectively.

The (kinetic) isotope fractionation associated with the Fe-Mg inter-diffusion was modeled by applying the following empirical formula (e.g., Richter et al. 1999):

$$\frac{D_q}{D_r} = \left(\frac{M_r}{M_q} \right)^\beta \quad (4)$$

where D represents the diffusion coefficient, q and r are isotopes of a certain element (e.g., ^{54}Fe and ^{56}Fe), and M is the atomic mass in a.m.u. The exponent β is an empirical constant and equal to 0.5 in ideal monoatomic gases (Van Orman and Krawczynski 2015). For olivine, β values appear to depend on crystal composition and diffusion direction relative to the orientation of the crystallographic axes (Van Orman and Krawczynski 2015) and, as the systematics of these dependencies is not clear yet, they are thus difficult to predict; however, they can be estimated by fitting observed isotope diffusion profiles across (natural) olivine crystals. Studies by Sio et al. (2013), Oeser et al. (2015), and Richter et al. (2016) indicate that β values for olivine fall in a range of 0.055–0.16 for Mg and of 0.075–0.30 for Fe. In this study, Fe and Mg isotopic profiles were fitted by adjusting the respective β values, i.e., modifying the diffusivity ratio of two isotopes of the same element (e.g., ^{54}Fe and ^{56}Fe) until the amplitude of

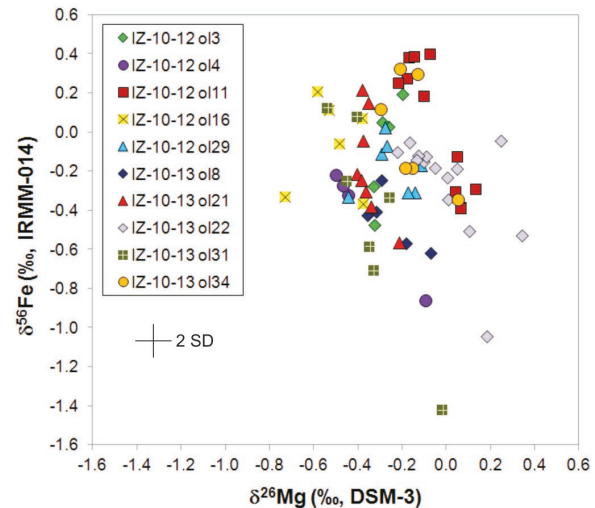


FIGURE 7. $\delta^{56}\text{Fe}$ and $\delta^{26}\text{Mg}$ values for all Fe-Mg isotopic profiles acquired in this study, illustrating that Fe isotope variations (up to 1.7‰) are much more pronounced than Mg isotope variations (<0.6‰) in all investigated olivine grains. (Color online.)

the modeled isotope fractionation matched that of the observed one. As a consequence, the used β values are purely empirical and characteristic for the given simulated case. In this study, β_{Fe} values used range from 0.12 to 0.25 (Table 1), and therefore fully agree with previous estimates of β_{Fe} in olivine (Sio et al. 2013; Oeser et al. 2015; Collinet et al. 2017).

DISCUSSION

Sequence of events recorded by complexly and normally zoned Irazú olivines

The zoning characteristics of type B olivines provide unique constraints on the spatial origin of these crystals and the temporal incorporation of different end-members into the eruption. As type A and type B crystals have a shared history within the outer zones of the crystals and type B olivines merge onto the general geochemical evolution recorded in type A olivines we suggest that the xenocrystic type B cores were remobilized in the crust by ascending mantle-derived melts carrying the magnesian type A olivines. This is evidence that the mixing event recorded by Ni zonation in magnesian type A olivines occurred at deeper levels than the storage depth of the xenocrystic type B olivines (which is likely to be >15 km beneath the volcano's summit based on the trace element characteristics of type B olivines; see below), further corroborating the assumption of near-Moho origin of the primitive type A olivines (Ruprecht and Plank 2013). In addition to the compositional differences, type B complex olivines are also not uniformly distributed within the 1963–65 eruption. Of the three samples studied in the past, IZ-10-11 (the earliest phase of the eruption studied by Ruprecht and Plank 2013) lacks significant amounts of type B olivines, while type A and C are both common. Type B olivines are most common in IZ-10-12, but also present in IZ-10-13, suggesting that the assembly of the 1963–65 eruption is complex where some components wane and wax.

The complex zoning of the Irazú type B olivines investigated in this study points to at least two episodes of crystal growth under diverse crystal-melt equilibrium conditions. The intermediate-Fo contents (Fo_{80-87}), high-Ni concentrations (2600–3200 ppm Ni), and anomalously high Ni-Cr ratios (Fig. 4) in the cores of these olivines indicate that these crystals were formed and equilibrated in the middle or lower crust beneath Irazú volcano, probably in a crystal mush or mafic cumulate (see section “Assembling the Irazú magma”). The Mg-rich zone near the rims of the complexly zoned olivines may then have formed by crystal growth when these crystals were entrained into ascending mantle melts and brought into the plumbing system in the shallow crust beneath Irazú volcano. The sharp intra-mineral chemical gradient produced by this second growth event was eventually smoothed out by Fe-Mg inter-diffusion as implied by the strong coupling of Fe-Mg chemical and isotopic zoning. Modeling this diffusive process (diffusion episode 1) therefore yields information about the time span from the entrainment of these olivines in the crust to the eruption. Previous studies have used similar Fe-Mg zoning patterns (initial step function, subsequent diffusive relaxation) in olivine to estimate mixing-to-eruption timescales by diffusion modeling (e.g., Kahl et al. 2011, 2013; Longpré et al. 2014; Hartley et al. 2016). However, all of these studies assumed that

the observed zoning was the result of instantaneous growth of a crystal layer with a different composition than the core and subsequent Fe-Mg inter-diffusion (cf. scenario 3 in Oeser et al. 2015), which provides maximum timescales. In this study, we additionally apply a model where crystal growth and Fe-Mg inter-diffusion occur simultaneously (scenario 4 in Oeser et al. 2015). As shown in Oeser et al. (2015), Fe-Mg isotopic profiles as obtained in this study can provide a further constraint upon which one of the two scenarios is more appropriate to describe the history recorded by intra-mineral zoning of olivine, leading to more reliable timescales obtained from diffusion modeling.

The similar zoning patterns at the rims of the complexly zoned olivines and of the primitive olivines ($\sim\text{Fo}_{88}$ to $\sim\text{Fo}_{80}$) from Irazú indicate that both crystal populations experienced a comparable late-stage history prior to the eruption. This likely included mixing with resident evolved magmas in the shallow crust as well as fractional crystallization from and, thus, further differentiation of the hybrid melt. The relative enrichment of light Fe and heavy Mg isotopes in the normally zoned part near the olivine rim implies that diffusive Fe-Mg exchange between crystal and melt represents the main process for the re-equilibration of olivine during that stage. It has to be noted that in some olivines the width of the normal zoning is so narrow that inversely correlated Fe-Mg isotopic profile cannot unambiguously be resolved by the LA technique used in this study, given the spatial resolution of 30–40 μm . However, olivines with wide normal zoning (e.g., IZ-10-13 ol22 and ol31 in Fig. 6 and Supplemental¹ Fig. S3, respectively) clearly show anti-correlated Fe-Mg isotopic profiles, which strongly argues for a diffusion origin of the normal zoning. As a consequence, we interpret this normal zoning to mainly be the result of a second diffusion episode (whose duration can be estimated by diffusion modeling) occurring in the shallow crust (shortly) prior to eruption.

Timescales of diffusion episodes

Diffusion episode 1. As described above, we applied two models to simulate the reverse zoning of the complexly zoned olivines (diffusion episode 1). The first one (instantaneous growth and subsequent Fe-Mg inter-diffusion) provides maximum timescales for the diffusive process, while in the second model (crystal growth and simultaneous Fe-Mg inter-diffusion) the shape of the simulated profiles depends on the timescale, as well as on the ratio of crystal growth rate (R in m/s) and diffusion coefficient of Fe-Mg diffusion in olivine (D in m^2/s ; see Supplemental¹ Fig. S5 for further details). Since D is determined by the chosen model parameters (T , P , f_{O_2} , etc.) and assumed to be identical in both models, the second model yields a timescale for the diffusive re-equilibration of the crystal and additionally the growth rate of the Mg-rich layer. Following the stepwise modeling approach presented in Kahl et al. (2011), the diffusion profiles generated during the first diffusion episode are used as the initial concentration (and isotopic) gradients for diffusion episode 2, which produced the normal zoning at the rims of the complexly zoned and primitive olivines investigated herein. Hence, the reverse zoning of diffusion episode 1 is not simulated to full completion, to allow for further relaxation during the second diffusion episode. The results of this diffusion modeling approach are shown in Tables 1 and 2, and representative

TABLE 1. Timescales of diffusive re-equilibration for complexly and normally zoned Irazú olivines, using a model of instantaneous growth and subsequent diffusion for diffusion episode 1 (t_1) if applicable

Sample	Type of Fe-Mg zoning	t_1 (days) ^a	t_2 (days) ^b	t_{total} (days) ^c	β_{Fe}	$\cos(\alpha)^2$	$\cos(\beta)^2$	$\cos(\gamma)^2$
IZ-10-12 ol3	complex	168	48	216	0.205	0.952	0.009	0.038
IZ-10-12 ol11	complex	533 ^d	56 ^d	589	0.220	0.900	0.086	0.014
IZ-10-12 ol16	complex	92	6	98	0.150	0.324	0.140	0.535
IZ-10-12 ol29	complex	151	11	162	0.180	0.045	0.755	0.200
IZ-10-13 ol21	complex	294	1456	1750	0.250	0.261	0.733	0.006
IZ-10-13 ol31	complex	126	448	574	0.220	0.638	0.313	0.050
IZ-10-13 ol34	complex	185	73	258	0.160	0.576	0.281	0.142
IZ-10-12 ol4	normal	x^e	168	168	0.120	0.514	0.436	0.050
IZ-10-13 ol8	(multiple) normal	x^e	112	112	0.150	0.735	0.215	0.051
IZ-10-13 ol22	normal	x^e	224	224	0.140	0.016	0.012	0.972

^a Model parameters for diffusion episode 1: $T = 1150$ °C, f_{O_2} at NNO+1, $X_{\text{Fe}} = 0.15$, $P = 500$ MPa.^b Model parameters for diffusion episode 2: $T = 1080$ °C, f_{O_2} at NNO+1, $X_{\text{Fe}} = 0.15$, $P = 100$ MPa.^c Given the uncertainties of the temperature estimation (± 50 °C), of the assumed f_{O_2} , and of the experimental calibration of $D_{\text{Fe-Mg}}$, the uncertainty of the modeled timescales is within a factor of four.^d Timescales obtained by fitting the width of the isotopic diffusion profile, as the Fe-Mg chemical diffusion profile appears to be distorted due to the polishing of the crystal before the EMPA.^e $x = \text{not applicable.}$ **TABLE 2.** Timescales of diffusive re-equilibration and integrated growth rates for complexly zoned Irazú olivines, using a model of growth and simultaneous diffusion for diffusion episode 1 (t_1)

Sample	Type of Fe-Mg zoning	t_1 (days) ^a	t_2 (days) ^b	t_{total} (days)	Growth rate (m/s) ^c	Pe^e
IZ-10-12 ol3	complex	128	48	176	1.0×10^{-11}	21
IZ-10-12 ol11	complex	530 ^d	56 ^d	586	3.0×10^{-12}	13
IZ-10-12 ol16	complex	90	6	96	1.3×10^{-11}	16
IZ-10-12 ol29	complex	110	11	121	9.5×10^{-12}	12
IZ-10-13 ol21	complex	290	1456	1746	1.0×10^{-11}	38
IZ-10-13 ol31	complex	110	448	558	2.1×10^{-11}	46
IZ-10-13 ol34	complex	180	73	253	9.9×10^{-12}	22

^a Model parameters for diffusion episode 1: $T = 1150$ °C, f_{O_2} at NNO+1, $X_{\text{Fe}} = 0.15$, $P = 500$ MPa.^b Model parameters for diffusion episode 2: $T = 1080$ °C, f_{O_2} at NNO+1, $X_{\text{Fe}} = 0.15$, $P = 100$ MPa.^c Rate of growth (R) of the Mg-rich layer during diffusion episode 1.^d Timescales obtained by fitting the width of the isotopic diffusion profile, as the Fe-Mg chemical diffusion profile appears to be distorted due to the polishing of the crystal before the EMPA.^e Peclet number ($R \cdot \Delta x / D$), where R is the growth rate, Δx is the zoning length scale, and D is the diffusion coefficient, for diffusion episode 1.

simulated diffusion profiles for four complexly zoned olivines are illustrated in Figures 8 to 11. Our results indicate that the duration of diffusion episode 1 was between ~ 90 and ~ 530 days (Table 1). These timescales imply that the transfer of material from the lower crust to the shallow plumbing system beneath an active volcano can occur in less than two years or even within a few months. This is consistent with observations made by Ruprecht and Plank (2013) for primitive magnesian olivines with reverse Ni zoning, which have been transported with mantle-derived magmas through the crust at an average rate of 50–80 m per day. The fact that the complexly zoned olivines still record quite a range of timescales of diffusive re-equilibration (90–530 days) may indicate (1) that not all of them were transported with the same mantle-derived magma batch, and/or (2) that they were picked up from various parts of the crust beneath Irazú volcano at different points in time. The latter possibility is supported by the fact that the cores of these olivines show a range of Fo compositions from Fo_{80} to Fo_{87} , along with some variability in Fe- and Mg-isotopic compositions, suggesting slightly different equilibration environments. Nevertheless, six out of the seven complexly zoned olivines investigated herein record diffusion timescales of less than 300 days for the first diffusion episode,

and thus a rapid transport into the shallow crust after being entrained into ascending mantle melts. These timescales are even shorter by up to $\sim 25\%$ if we assume that the growth of the Mg-rich layer and the diffusive equilibration of this intra-mineral chemical gradient occurred simultaneously during diffusion episode 1 (Table 2). Coeval growth and diffusion could also explain slight offsets (within ~ 30 μm) of the profile step locations for different elements required to fit Fe-Mg, Cr, V, and Al zoning profiles. Unfortunately, neither the elemental zoning nor the Fe(-Mg) isotopic profiles can unequivocally unravel which of the two scenarios is the more likely one for the investigated olivines, i.e., both models (instantaneous growth + subsequent diffusion vs. growth + simultaneous diffusion) yield equally good fits for the Fe isotopic profiles in most olivines (Fig. 10). Only for one crystal (IZ-10-12 ol29) the second model reproduces the Fe isotopic profile much better (Fig. 11). The fairly good fits that are obtained if the first model (instantaneous growth + subsequent diffusion) is applied, indicate that assumptions made in previous studies for similar Fe-Mg chemical profiles in olivine (e.g., Kahl et al. 2011; Longpré et al. 2014; Hartley et al. 2016) are reasonable (see above). In other words, based on the observations of this study, potential simultaneous crystal growth and diffusion appears to play a minor role in modifying Fe-Mg chemical and isotopic gradients in olivine. Nevertheless, only the combination of in situ Fe-Mg concentration and isotopic analyses in olivine is capable of unraveling such complex growth + diffusion histories.

As described above, our second model (growth + simultaneous diffusion) does not only provide a timescale for the diffusion process, but also a growth rate for the Mg-rich layer. Based on the diffusion profiles observed in this study, these growth rates range from 3×10^{-12} to 2×10^{-11} m/s (Table 2). Compared to experimentally determined growth rates of olivines in basaltic melts (10^{-10} to 10^{-7} m/s, Donaldson 1975; Jambon et al. 1992), such growth rates seem to be exceptionally low. However, in natural systems olivine growth rates of 10^{-11} to 10^{-9} m/s appear to be more realistic (Maaløe 2011; Watson et al. 2015), probably due to a smaller degree of supercooling prevailing under natural conditions (cf. Jambon et al. 1992), and/or due to a decrease in the degree of supersaturation with time in a natural magma reservoir (cf. Maaløe 2011), which is

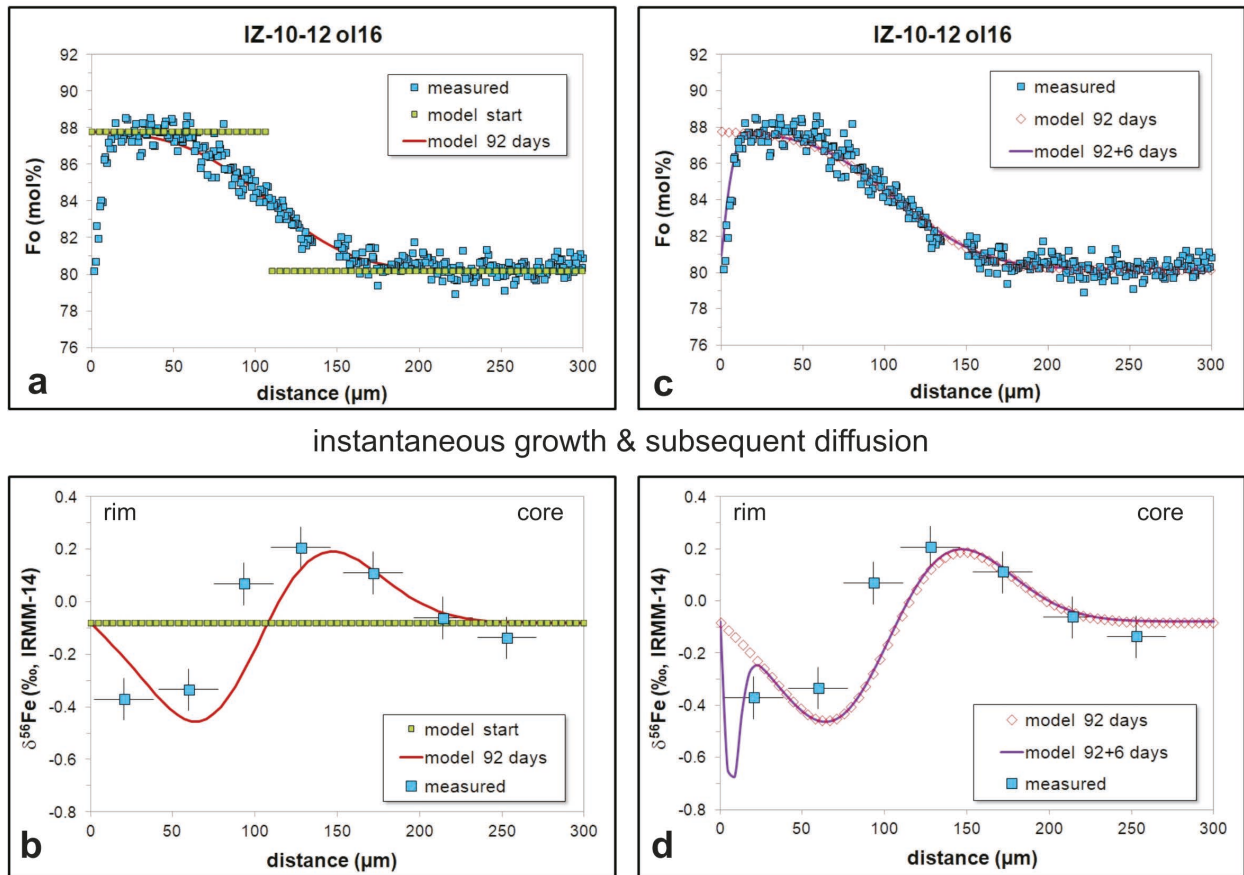


FIGURE 8. Results of the stepwise diffusion modeling approach used in this study for a complexly zoned olivine (IZ-10-12 ol16). Profile of Fo contents is based on the calibrated BSE (grayscale) image of this crystal. (**left**) Subfigures show the measured and modeled Fo contents (**a**) and the measured and modeled Fe isotopic compositions (**b**) for diffusion episode 1, assuming a model of instantaneous growth of a Mg-rich layer (distance 0–106 μm in **a**) and subsequent Fe-Mg inter-diffusion. For diffusion episode 2 (**right**), the diffusion profiles generated during the first diffusion episode are used as the initial concentration (and isotopic) gradients, and only the rim composition (at distance = 0 μm) is modified to simulate diffusion of Fe into (and Mg out of) the olivine. (Color online.)

less pronounced in experimental studies because of the limited runtime of the experiments.

Diffusion episode 2. The second diffusion episode, which generated the normally zoned rims of the complexly zoned and the primitive olivines investigated herein, lasted between a few days and \sim 450 days (Tables 1 and 2). One olivine records an exceptionally long timescale of diffusive re-equilibration in the second diffusion stage (\sim 1450 days, IZ-10-13 ol21). It has to be noted again that these timescales—as well as the timescales for diffusion episode 1—likely represent maximum estimates since we assume that the observed normal zoning is purely diffusion-generated (as implied by the inversely correlated Fe-Mg isotopic profiles, Fig. 6) and that the investigated olivines do not contain significant amounts of H^+ (which would strongly enhance $D_{\text{Fe-Mg}}$; e.g., Hier-Majumder et al. 2005). However, we cannot exclude that crystal growth during fractional crystallization and further differentiation of the melt also had some influence on the development of that normal zoning, especially near the surface where cooling and partial degassing drive crystallization more effectively. Unfortunately, the spatial resolution of the LA technique

used in this study is not sufficient to resolve the extent of this influence. As a consequence, we prefer to provide conservative, i.e., maximum, estimates for the timescales of processes beneath Irazú volcano. The variability of observed diffusion times for diffusion episode 2 may be an indication of a complex plumbing system beneath Irazú volcano where various crystal populations are stored in diverse magma batches for a certain amount of time before eruption. Still, short diffusion timescales, i.e., <200 days, appear to prevail, implying that magma mixing events in the shallow crust and following eruptions take place within a matter of months, if not days.

Mixing-to-eruption times and magma ascent rates. The stepwise modeling approach applied in this study (see above) also allows us to estimate the time spans between the entrainment of the complexly zoned olivines into ascending mantle melts and the eruption (t_{total} in Tables 1 and 2). These timescales range from \sim 100 to \sim 1750 days, with short timescales of <600 days ($n = 6$) being more common than longer ones ($n = 1$). Assuming that these crystals were picked up somewhere in the middle crust, i.e., \sim 15 km beneath the volcano's summit, given a crustal thick-

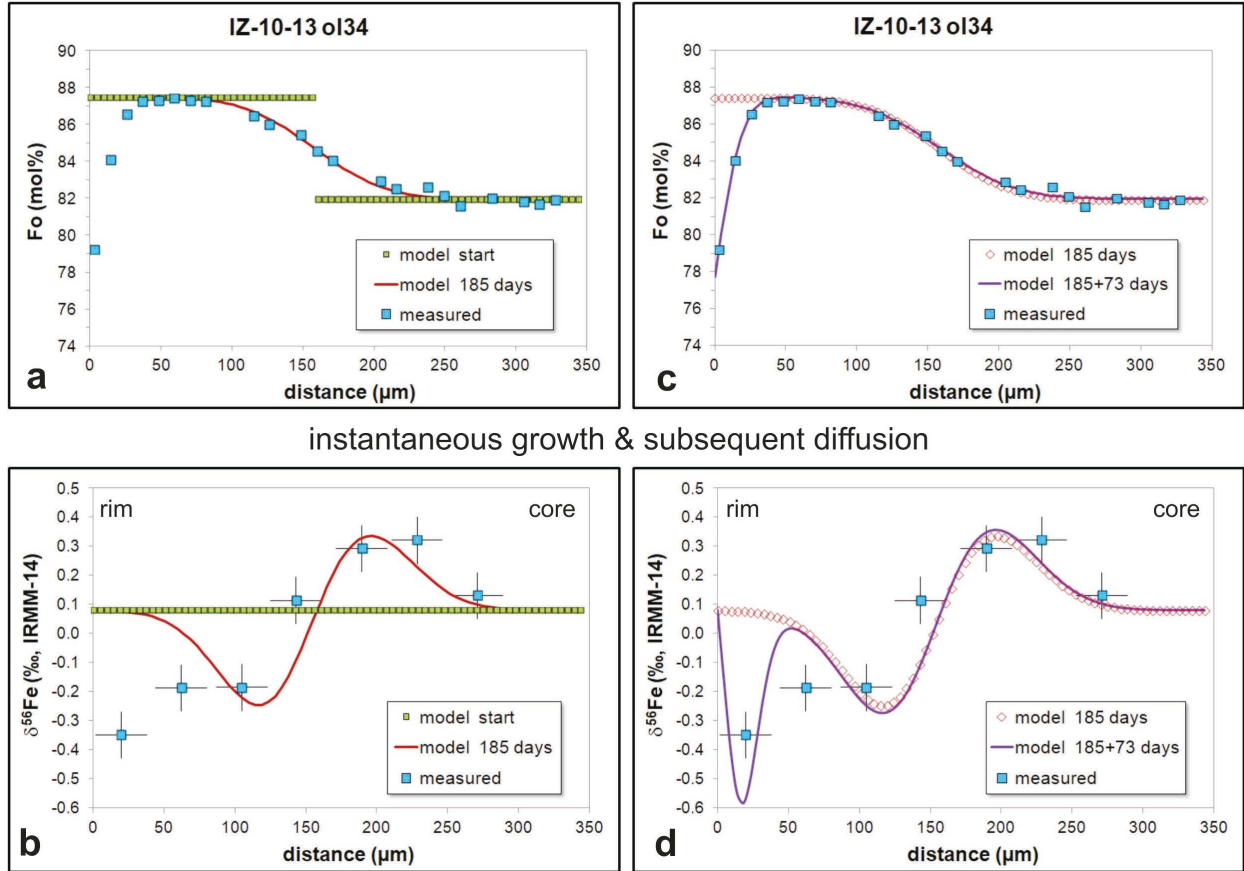


FIGURE 9. Results of the stepwise diffusion modeling approach used in this study for a complexly zoned olivine (IZ-10-13 ol34), assuming a model of instantaneous growth of a Mg-rich layer (distance 0–156 μm in **a**) and subsequent Fe-Mg inter-diffusion for diffusion episode 1 (**left**). This example also illustrates that the second diffusion episode (**right**) with diffusion of Fe into (and Mg out of) the olivine is needed to reproduce the low-Fo content (**c**) and relative enrichment of light Fe isotopes (**d**) near the rim. Note that the profile of Fo contents is shown as measured by EMPA. For further details, see figure caption of Figure 8. (Color online.)

ness of \sim 35 km (Dzierma et al. 2010), the average ascent rate of the magmas carrying these olivines through the crust would be 25 m per day. Again, this represents a conservative estimate as (1) several olivines record mixing-to-eruption timescales much shorter than 600 days, and (2) the complexly zoned olivines may have been entrained into ascending mantle melts at greater depth, i.e., >15 km beneath the volcano's summit (see above). Also, such rates are averages, while transient transport rates are likely much faster (e.g., Rubin 1995). Nevertheless, an average ascent rate of 25 m/day is largely consistent with magma ascent rates of 50–80 m/day determined by Ruprecht and Plank (2013) based on diffusion modeling of reverse Ni zoning in magnesian olivines from the same sample suite and using a temperature range of 1100 to 1200 $^{\circ}\text{C}$.

Uncertainties of the modeled timescales. As illustrated in, e.g., Oeser et al. (2015) and Kahl et al. (2015), uncertainties of timescales calculated by Fe-Mg diffusion modeling mainly result from the uncertainty of temperature estimations. In our case, we chose a temperature of 1150 $^{\circ}\text{C}$ for diffusion episode 1 that is well within the range of reported pre-eruptive temperatures of basalts from Irazú volcano (Alvarado et al. 2006). If this assumption

was incorrect, and the temperature was 50 $^{\circ}\text{C}$ lower (or higher), the timescales obtained from diffusion modeling for diffusion episode 1 would be longer (or shorter) by a factor of \sim 2.4. For diffusion episode 2, we assumed a temperature of 1080 $^{\circ}\text{C}$, based on olivine-melt thermometry for basaltic andesites erupted from Irazú in 1723 (Benjamin et al. 2007). If this temperature was actually 50 $^{\circ}\text{C}$ lower for the samples investigated in our study (basaltic andesites erupted in 1963–65), the timescales obtained from diffusion modeling for diffusion episode 2 would be longer by a factor of \sim 2.6. As summarized in Costa et al. (2008), at any given temperature the uncertainty of $D_{\text{Fe-Mg}}$ resulting solely from the experimental calibration is a factor of \sim 2. Incorrect assumptions for the oxygen fugacity prevailing during the diffusion stages may also lead to over- or underestimations of diffusion times (Oeser et al. 2015); however, these are minor compared to those arising from errors of temperatures estimates. For example, if the oxygen fugacity was at $\Delta\log f_{\text{O}_2}$ (NNO) = 0 (instead of +1 as presumed in our model) during diffusion episode 1, modeled timescales would be longer by a factor of \sim 1.5. Given these uncertainties, we are confident that the overall uncertainty of the timescales determined by diffusion modeling in this study is not larger than

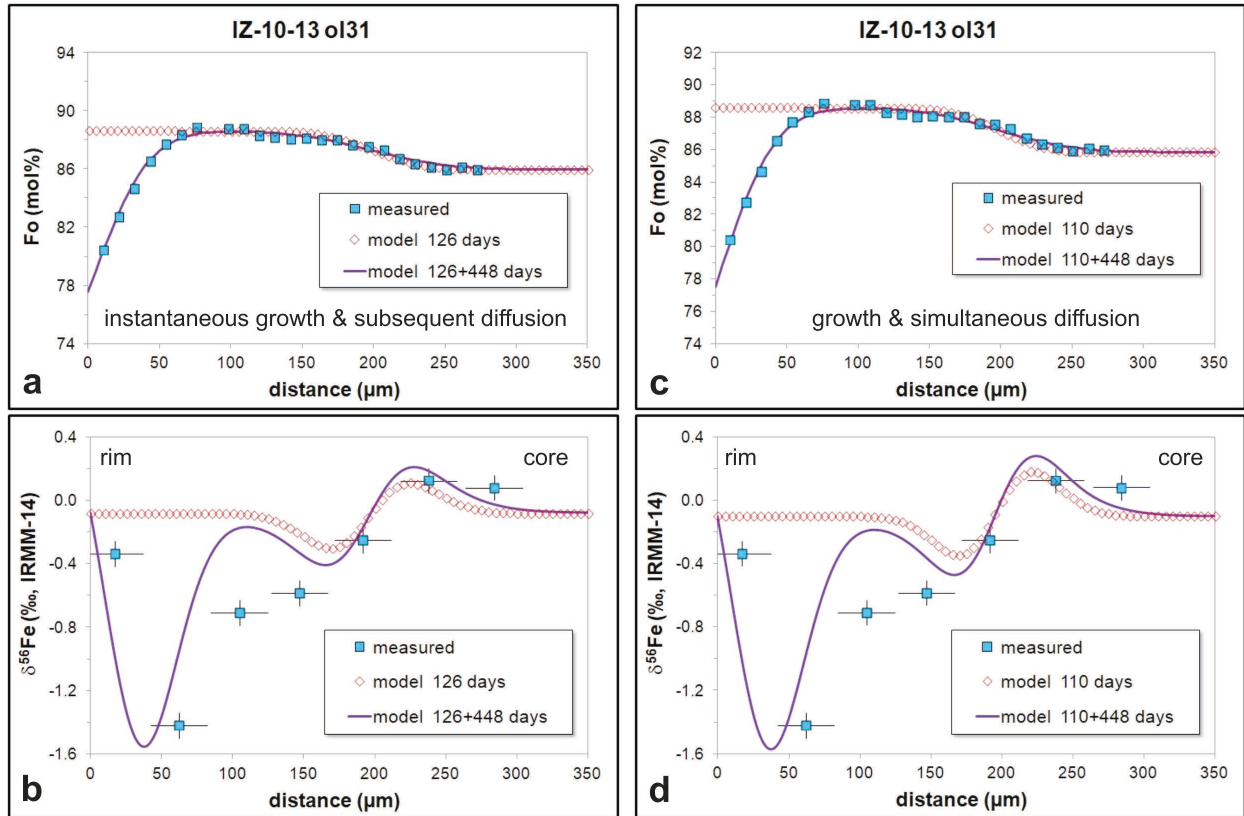


FIGURE 10. Comparison of modeling results obtained from two models for diffusion episode 1 [instantaneous growth and subsequent diffusion (left) vs. growth and simultaneous diffusion (right)], both of which are followed by simple diffusive Fe-Mg exchange between crystal and melt (diffusion episode 2, lasting 448 days in this case). Both models for diffusion episode 1 are able to reproduce the Fe-Mg chemical (a and c) and Fe isotopic zoning (b and d) of this olivine reasonably well. (Color online.)

a factor of four, which is typical for the calculation of timescales from diffusion modeling in magmatic systems (Costa et al. 2008).

Assembling the Irazú magma prior to the 1963–65 eruption

The new results from Fe-Mg isotopes generally corroborate the timescales of magma transport through the crustal magma system (Ruprecht and Plank 2013). By expanding our analysis to crystals with intermediate-Fo, high-Ni cores we can provide a more complete picture of the architecture of the magma system beneath Irazú and the assembly of the magma prior to the 1963–65 eruption (Fig. 12). Comparison with other crustal cumulate olivine data from crustal sections (e.g., Otamendi et al. 2016) suggests that the intermediate-Fo, high-Ni cores are not simple olivine phenocrysts that represent a different magma batch in the crust. Instead, they are best explained as xenocrystic olivine that was picked up by the primitive magma as it intersected an olivine cumulate. The high Ni/Cr ratio in these cores are consistent with this interpretation and suggest that during olivine cumulate formation pyroxenes co-crystallized and through time both mineral phases equilibrated so that Ni was incorporated into the olivine at the expense of pyroxene and Cr behaves in reverse being concentrated in the pyroxenes. Typical distribution coefficients for Cr and Ni between olivine and clinopyroxene are <0.01 and ~ 4 , respectively (Otamendi

et al. 2016). The observed concentrations are consistent with this model as Cr content in the xenocrystic cores is one to two orders of magnitude lower than in common olivines and Ni is about a factor of 2 higher.

Our model suggests that the primitive magma intersected a mafic (maybe ultramafic) crustal cumulate on its way to the surface. The fact that olivine cores are overgrown by primitive Ni-rich, high-Fo mantles further indicates that this contamination of the erupted magma occurred at a depth well below the shallow Irazú magma plumbing system. We have not attempted to estimate the depth for this cumulate, but comparing our results to a crustal section study that exposes olivine cumulates of similar geochemical characteristics within the section suggests at least mid-crustal levels (>15 km depth; Otamendi et al. 2016) and potentially lower crustal conditions. Those depths/pressures are constrained through phase assemblages and compositions studied in this crustal section. Irrespective of the exact location of olivine cumulate contamination, crystal zoning correlations between type A and type B olivines provides evidence that the primitive high-Fo olivines must originate from greater depth and likely crystallized near the Moho (as it was previously postulated by Ruprecht and Plank 2013), precluding aphyric magma ascent of primitive melts to shallow levels with ensuing crystallization near the shallow crustal magma reservoirs (Fig. 12).

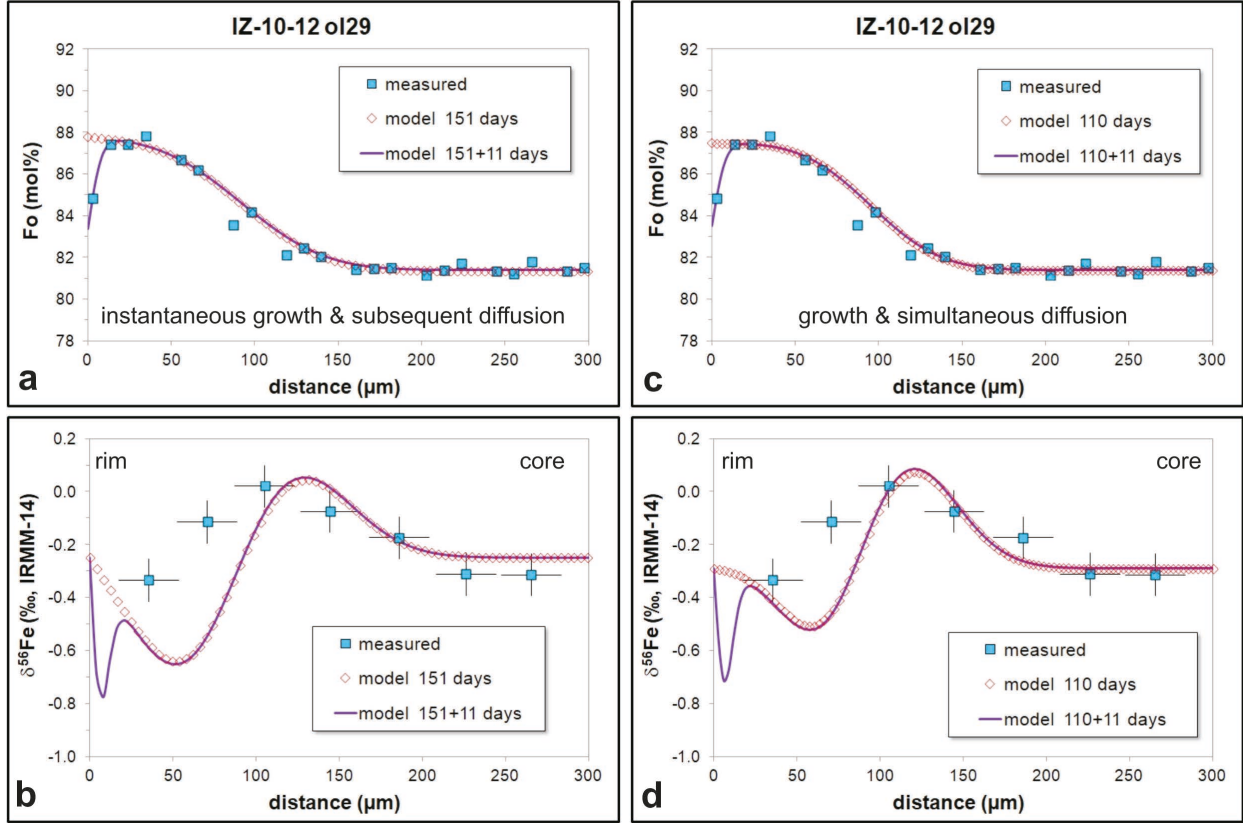


FIGURE 11. Comparison of modeling results obtained from two models for diffusion episode 1 [instantaneous growth and subsequent diffusion (left) vs. growth and simultaneous diffusion (right)], both of which are followed by simple diffusive Fe-Mg exchange between crystal and melt (diffusion episode 2, lasting 11 days in this case). Both models for diffusion episode 1 are able to reproduce the Fe-Mg chemical zoning of this olivine (a and c); however, the second model yields a much better fit to the Fe isotopic zoning of this crystal (d), indicating that the shorter diffusion timescale (110+11 days) is more likely in this case. (Color online.)

Diffusion of chromium in olivine

The coupling of Fe-Mg isotope and elemental zoning results provide valuable constraints for the growth and diffusion history of the Irazú olivines. As indicated by the Fe-Mg isotopic zoning, chemical zoning was essentially driven by chemical diffusion following rapid (near instantaneous) growth. This finding allows to utilize Irazú olivines to calculate relative diffusion coefficients for Cr, Al, and V. We focus on Cr, Al, and V diffusivities as those are much less understood than divalent minor and major elements in olivine (Fe-Mg, Mn, Ca, Ni). In particular, Cr and Al diffusivities have been argued to vary over orders of magnitude (Cr: Ito and Ganguly 2006; Spandler and O'Neill 2010; Jollands et al. 2018; Al: Milman-Barris et al. 2008; Spandler and O'Neill 2010; Zhukova et al. 2017). The variations in Cr diffusion have been reconciled recently by Jollands et al. (2018) recognizing that low- a_{SiO_2} systems (Ito and Ganguly 2006) may show slow Cr diffusion, while high- a_{SiO_2} systems near the olivine-enstatite buffer (Spandler and O'Neill 2010) lead to significantly faster Cr diffusion. Moreover it was documented that Cr diffusion is strongly concentration dependent (Jollands et al. 2018), an effect that cannot be explored in this study meaningfully.

We do not attempt to estimate specific diffusivities for a

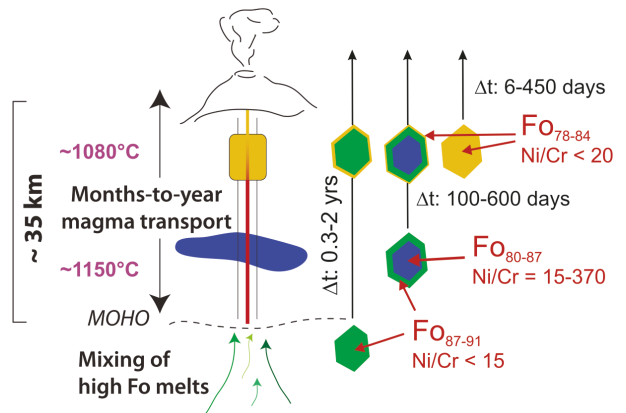


FIGURE 12. Schematic architecture of Irazú magma system (modified from Ruprecht and Plank 2013) with information about major and trace element characteristics of the three main olivine types and about timescales of transport (Δt) as deduced in this study from diffusion modeling at the given temperature range (1080–1150 °C). Transport timescale for primitive magnesian olivines (green) from MOHO depth is from Ruprecht and Plank (2013), based on diffusion modeling of reverse Ni zoning. (Color online.)

specific temperature as we think that there are still significant uncertainties with the analysis of these natural olivines. Neither temperature nor oxygen fugacity in the Irazú magmatic system (thought to be near NNO+1, Benjamin et al. 2007, setting valence states of predominantly Cr^{3+} and V^{4+} , Papike et al. 2005; Mallmann et al. 2009) is tightly constrained when compared to experimental studies. However, as chemical zoning is primarily a result of chemical diffusion and not growth for the investigated olivine crystals, we can determine Cr and, with a higher uncertainty, V and Al diffusion relative to each other and to that of experimentally well-determined Fe-Mg inter-diffusion (Fig. 13).

For this approach to produce meaningful diffusivity estimates, we assume that the zoning profile in the olivines is generated by diffusion following a rapid growth period that generated a step function as starting conditions for diffusion and therefore represents a maximum diffusivity estimate. The previously discussed Fe-Mg isotope zoning supports in general this diffusion-dominated regime for the studied olivines. Second, to extract diffusivity information on these elements one has to ensure that the finite (measured) length scale of the zoning profiles is primarily a true (diffusion-generated) zoning profile in the crystals and not an artifact of the acquisition method using a scanning laser with a continuous time series. The laser spot size of 25 μm and the continuous sample movement underneath the laser intrinsically creates zonation patterns with a measurable length scale, where even true step functions would be smeared to resemble an evolving diffusion profile (Bradshaw and Kent 2017; Supplemental¹ Fig. S6). With increasing diffusion length scale

(e.g., due to increasing diffusivity, Supplemental¹ Fig. S6) zoning profiles acquired during laser ablation and the true zoning profiles converge, and the sampling bias by a continuously moving laser track becomes negligible. To quantitatively compare true zoning and laser-generated profiles we extrapolate the maximum slope at the center where the curvature of the profile changes signs to the concentration plateaus of the step functions and obtain a conservative estimate Δx for the diffusion profile length for all elements of interest (Supplemental¹ Fig. S7, Supplemental¹ Table S4). Comparing the apparent diffusivity as a function of the lengthscale Δx one can see that as Δx approaches the spot size (25 μm) the profile cannot be resolved unambiguously and any calculated diffusivity becomes increasingly overestimated. We can correct for this effect by calculating a smearing factor that accounts for the laser-generated smearing effects. All reported length scales Δx for all elements (Supplemental¹ Table S4) are significantly larger than the minimum spatial resolution, thus supporting the notion that these profiles are not simple step functions. As a result we can estimate diffusivities and apply a correction factor for the smearing that varies between 1.399 ($\Delta x = 32 \mu\text{m}$) and 1.071 ($\Delta x = 71 \mu\text{m}$). No correction was applied for zoning length scales $>100 \mu\text{m}$ as our analysis was limited to $\Delta x < 100 \mu\text{m}$ and the polynomial approximation is overestimating the smearing effect for large Δx . Last, we neglect potential effects of off-perpendicular (relative to the crystal-melt interface) sectioning of the crystals. Imaging of the crystals prior to and after LA-ICP-MS analysis, after polishing (typically removal of $\sim 10-20 \mu\text{m}$) prior to MC-ICP-MS analysis, and again after

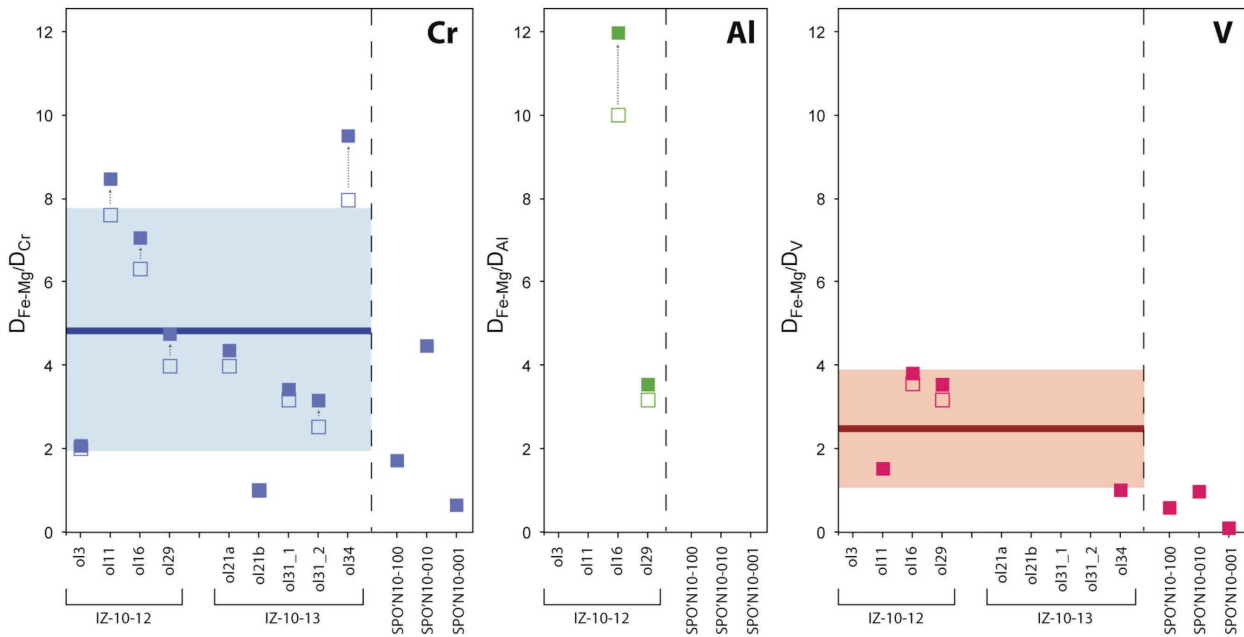


FIGURE 13. Comparison of Cr, Al, and V diffusivity relative to Fe-Mg inter-diffusion. Filled and open squares are results for smearing corrected and uncorrected profiles, respectively. Al data are limited to sample IZ-10-12, which was measured on a day with better instrument sensitivity. The results for Cr and V diffusivity determined by Spandler and O'Neill (2010; SPO'N10) are shown for comparison, whereas Al diffusion was not quantified in that study. Experiments on Cr diffusion by Jollands et al. (2018) did not explore coexisting Fe-Mg inter-diffusion and therefore no diffusivity ratios are shown for this study. The results from our study are not plotted for specific crystallographic axis, because of random orientations of the diffusion profiles; see supplementary data (Supplemental¹ Table S3) for rotation angles. Diffusivities were determined by 1D diffusion profiles (see Fig. 14). (Color online.)

polishing post MC-ICP-MS analysis shows that zoning evolution into the Z-direction of the crystal is persistent and crystal shapes in general change only to a small degree. This suggests that crystal sectioning was close to perpendicular relative to the crystal-melt interface for most crystals. In summary, the calculated zoning lengthscales and crystal imaging suggest that the profiles represent gradational zoning in Cr content from core to rim and, together with the Fe-Mg isotope zoning record, we can estimate elemental diffusivities for selected elements.

After the smearing correction is applied we find that $D_{\text{Fe-Mg}} > D_{\text{V}} > D_{\text{Cr}} > D_{\text{Al}}$. Our most robust results—given that we find similar diffusivities for 7 crystals and 9 different traverses (Figs. 13 and 14; Supplemental¹ Fig. S8)—are for D_{Cr} , which is smaller than $D_{\text{Fe-Mg}}$ by a factor of 4.9 ± 2.9 , with the uncertainty representing 1 SD (standard deviation) of the calculated

population of diffusion coefficients. Therefore, the results from these natural olivines are consistent with fast Cr diffusion under high- a_{SiO_2} conditions (Spandler and O'Neill 2010; Jollands et al. 2018). Al and V are less well constrained, because zoning profiles are not consistently correlated with Fo content and, in the case of Al, our analytical uncertainties were high relative to Cr concentrations in all of our IZ-10-13 olivines. Nonetheless, the two olivine crystals for which Al zoning was distinct suggest that Al diffusivity may still be faster than inferred from other studies (Milman-Barris et al. 2008; Spandler and O'Neill 2010) consistent with results for Al diffusion in olivine under high a_{SiO_2} (Zhukova et al. 2017). A more extensive analysis will be required in the future, especially given that the comparison (Fig. 13) with data from Spandler and O'Neill (2010) is done at different temperatures. While our diffusivity ratios are calculated for a

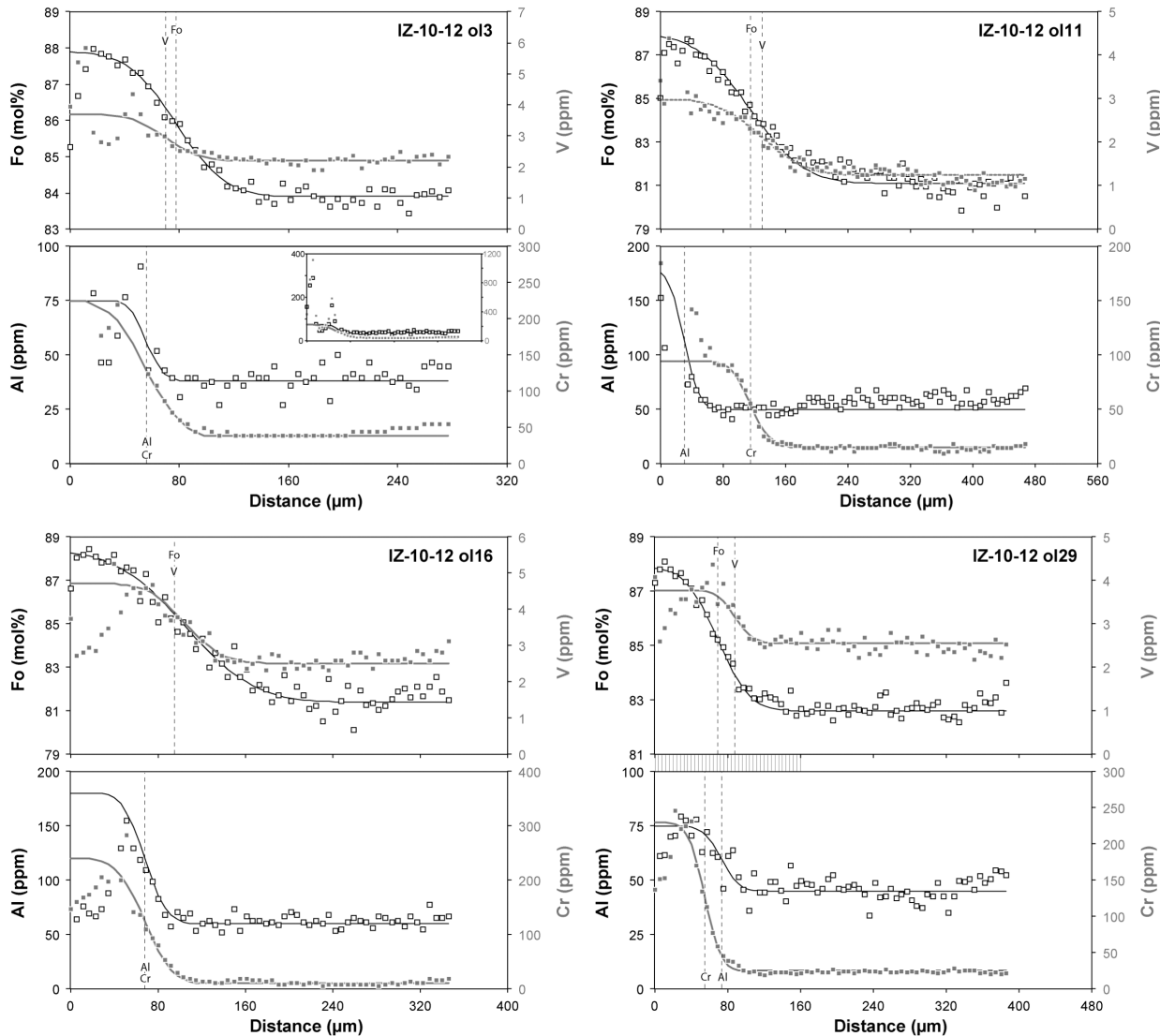


FIGURE 14. LA-ICP-MS rim-to-center analyses for Fo and Al (white squares) as well as Cr and V (gray squares). Calculated diffusion profiles used for the relative determination of elemental diffusivities are shown as black (Fo, Al) and gray (Cr, V) lines. Profiles were calculated separately for each element with a step profile. Step location was chosen to minimize misfit for the respective element. Near-rim zoning is ignored as it probably includes effects of fractional crystallization. Additional Fo, V, and Cr zoning profiles are shown in the supplementary material (Supplemental¹ Fig. S8).

temperature of about ~ 1150 °C, Spandler and O'Neill (2010) ran their experiments at 1300 °C. Thus, potential differences in the activation energy ([~ 200 kJ/(mol K) for Fe-Mg inter-diffusion in olivine, Dohmen et al. 2007; >300 kJ/(mol K) for Cr in olivine, Ito and Ganguly 2006; Jollands et al. 2018] are not accounted for in this comparison. The lower activation energy for Fe-Mg inter-diffusion suggests that $D_{\text{Fe-Mg}}/D_{\text{Cr}}$ should increase with lower temperatures as Cr diffusion is slowed more effectively at low T . Last, V diffusivity, as determined by the zoning profiles of only four olivine crystals (Figs. 13 and 14), is smaller than $D_{\text{Fe-Mg}}$ by a factor of 2.5 ± 1.4 . However, the activation energy for V diffusion is not known and an analysis for different temperatures cannot be performed. Given that V will not only be present as tetravalent species in terrestrial magmas, but also to some degree trivalent (Papike et al. 2005; Mallmann et al. 2009) it will require more experimental work to fully characterize V diffusion in olivine under common oxygen fugacities.

These results for diffusivities in olivine of selected tri- and tetravalent cations are, with the exception of Al, in good agreement with those of the previous study of Spandler and O'Neill (2010) who also did not provide diffusivities for a range of temperatures, but limited their experimental investigation to 1300 °C using San Carlos olivine (Fig. 13). In the latter study the authors had excellent crystallographic control and provided diffusivity estimates for all three crystallographic orientations and all their diffusivities are of similar order of magnitude to diffusivities from this study. The olivines in this study experienced lower temperatures (<1200 °C, see Ruprecht and Plank 2013, for additional discussion on this) compared to that of the experimental study of Spandler and O'Neill (2010). Both studies utilized natural olivines, and the San Carlos olivines as well as the overgrowth mantles in the Irazú olivines have high-Fo contents of $\sim \text{Fo}_{90}$. However, given the limitations of our analysis, the determined diffusivities represent maximum diffusivity estimates and while they overlap with experimental results (Spandler and O'Neill 2010; Jollands et al. 2018) this agreement may break down if any made assumption is not maintained. The result would be smaller diffusivities. Given the good agreement however and the fact that a_{SiO_2} (e.g., Jollands et al. 2018) is a likely factor controlling the differences in diffusivities suggest that our analysis is robust. Nonetheless, additional similar studies on natural samples, together with experimental studies, may enable to elucidate reasons for a range in diffusivity for specific elements.

IMPLICATIONS

The findings of this study demonstrate that a combination of Fe-Mg chemical and isotopic profiles in complexly zoned olivines provides reliable information on the origin of zoning and, thus, enables the unraveling of complex crystal growth and diffusion histories. This information can be used to optimize diffusion modeling to estimate the timescales of magmatic processes. In the case of olivines from Irazú volcano, such diffusion modeling yields the time span for the transfer of material from the middle or lower crust to the shallow plumbing system (<300 days for 6 out of 7 olivine crystals), but also magma mixing-to-eruption timescales. These are in good agreement with the timescales of ascent of mantle-derived magmas, as determined by diffusion modeling of Ni zoning in primitive olivines (Ruprecht and Plank

2013). Mixing-to-eruption times for crustal olivines beneath the continental arc volcano Irazú appear to be short (<600 days in most cases)—despite a magma storage region in the shallow crust—and thus imply that material from the lower or middle crust can be transported to the shallow plumbing system and eventually to the vent of an arc volcano while the eruption is already underway.

Xenocrystic olivines may provide independent constraints on the diffusivity of commonly slow-diffusing elements such as Cr and Al for which the determination of diffusivities by experimental approaches is challenging. However, analysis of Irazú olivines with xenocrystic cores and Cr zoning suggests that under those natural conditions Cr diffusion in olivine may be faster than previously determined by experiments. Additional studies are required to fully understand the mechanisms of Cr diffusion and whether elevated trace impurities and defects or the chemical activity of major elements are causing the enhanced diffusivity, as suggested for other elements and in olivine and other phases (e.g., Zhukova et al. 2014; Ferriss et al. 2016; Jollands et al. 2018).

ACKNOWLEDGMENTS

This study was supported by the project funding program “Wege in die Forschung II” of the Leibniz Universität Hannover. P.R. acknowledges support from the U.S. National Science Foundation (EAR 1426820/1719687). We are grateful to M. Jollands and C. Sio for very constructive reviews and we thank R. Almeev for efficient editorial handling.

REFERENCES CITED

Alvarado, G.E., Carr, M.J., Turrin, B.D., Swisher, C.C., Schmincke, H.-U., and Hudnut, K.W. (2006) Recent volcanic history of Irazú volcano, Costa Rica: Alternation and mixing of two magma batches, and pervasive mixing. Geological Society of America Special Papers, 412, 259–276.

Benjamin, E.R., Plank, T., Wade, J.A., Kelley, K.A., Hauri, E.H., and Alvarado, G.E. (2007) High water contents in basaltic magmas from Irazú Volcano, Costa Rica. Journal of Volcanology and Geothermal Research, 168, 68–92.

Bradshaw, R.W., and Kent, A.J.R. (2017) The analytical limits of modeling short diffusion timescales. Chemical Geology, 466, 667–677.

Carr, M.J. (1984) Symmetrical and segmented variation of physical and geochemical characteristics of the Central American Volcanic Front. Journal of Volcanology and Geothermal Research, 20, 231–252.

Chakraborty, S. (1997) Rates and mechanisms of Fe-Mg interdiffusion in olivine at 980°–1300°C. Journal of Geophysical Research, 102, 12,317–12,331.

— (2010) Diffusion coefficients in olivine, wadsleyite and ringwoodite. Reviews in Mineralogy and Geochemistry, 72, 603–639.

Collinet, M., Charlier, B., Namur, O., Oeser, M., Médard, E., and Weyer, S. (2017) Crystallization history of enriched shergottites from Fe and Mg isotope fractionation in olivine megacrysts. Geochimica et Cosmochimica Acta, 207, 277–297.

Costa, F., and Chakraborty, S. (2004) Decadal time gaps between mafic intrusion and silicic eruption obtained from chemical zoning patterns in olivine. Earth and Planetary Science Letters, 227, 517–530.

Costa, F., and Dungan, M. (2005) Short time scales of magmatic assimilation from diffusion modeling of multiple elements in olivine. Geology, 33, 837–840.

Costa, F., Dohmen, R., and Chakraborty, S. (2008) Time scales of magmatic processes from modeling the zoning patterns of crystals. Reviews in Mineralogy and Geochemistry, 69, 545–594.

Crank, J. (1975) The Mathematics of Diffusion, 2nd ed., 421 p. Clarendon Press, Oxford.

Dohmen, R., and Chakraborty, S. (2007) Fe-Mg diffusion in olivine II: Point defect chemistry, change of diffusion mechanisms and a model for calculation of coefficients in natural olivine. Physics and Chemistry of Minerals, 34, 409–430.

Donaldson, C.H. (1975) Calculated diffusion coefficients and the growth rate of olivine in a basalt magma. Lithos, 8, 163–174.

Dzierma, Y., Thorwart, M.M., Rabbel, W., Flueh, E.R., Alvarado, G.E., and Mora, M.M. (2010) Imaging crustal structure in south central Costa Rica with receiver functions. Geochemistry, Geophysics, Geosystems, 11, 1–21.

Ferriss, E., Plank, T., and Walker, D. (2016) Site-specific hydrogen diffusion rates during clinopyroxene dehydration. Contributions to Mineralogy and Petrology, 171, 1–24.

Gazel, E., Hayes, J.L., Hoernle, K., Kelemen, P., Everson, E., Holbrook, W.S., Hauff, F., van den Bogaard, P., Vance, E.A., Chu, S., and others. (2015) Continental crust generated in oceanic arcs. Nature Geoscience, 8, 321–327.

Global Volcanism Program (2013) Irazú (345060). In E. Venzke, Ed., Volcanoes of the

World. Smithsonian Institution, <http://volcano.si.edu/volcano.cfm?vn=345060>.

Hartley, M.E., Morgan, D.J., MacLennan, J., Edmonds, M., and Thordarson, T. (2016) Tracking timescales of short-term precursors to large basaltic fissure eruptions through Fe-Mg diffusion in olivine. *Earth and Planetary Science Letters*, 439, 58–70.

Hier-Majumder, S., Anderson, I.M., and Kohlstedt, D.L. (2005) Influence of protons on Fe-Mg interdiffusion in olivine. *Journal of Geophysical Research B: Solid Earth*, 110, 1–12.

Ito, M., and Ganguly, J. (2006) Diffusion kinetics of Cr in olivine and ^{53}Mn - ^{53}Cr thermochronology of early solar system objects. *Geochimica et Cosmochimica Acta*, 70, 799–809.

Jambon, A., Lussiez, P., Clocchiatti, R., Weisz, J., and Hernandez, J. (1992) Olivine growth rates in a tholeiitic basalt: An experimental study of melt inclusions in plagioclase. *Chemical Geology*, 96, 277–287.

Jarosewich, E., Nelen, J.A., and Norberg, J.A. (1980) Reference samples for electron microprobe analysis. *Geostandards Newsletter*, 4, 43–47.

Jollands, M.C., O'Neill, H.St.C., and Hermann, J. (2014) The importance of defining chemical potentials, substitution mechanisms and solubility in trace element diffusion studies: the case of Zr and Hf in olivine. *Contributions to Mineralogy and Petrology*, 168, 1055.

Jollands, M., Hermann, J., O'Neill, H.St.C., Spandler, C., and Padrón-Navarta, J.A. (2016a) Diffusion of Ti and some divalent cations in olivine as a function of temperature, oxygen fugacity, chemical potentials and crystal orientation. *Journal of Petrology*, 57, 1983–2010.

Jollands, M.C., Burnham, A.D., O'Neill, H.St.C., Hermann, J., and Qian, Q. (2016b) Beryllium diffusion in olivine: A new tool to investigate timescales of magmatic processes. *Earth and Planetary Science Letters*, 450, 71–82.

Jollands, M.C., O'Neill, H.St.C., Van Orman, J., Berry, A.J., Hermann, J., Newville, M., and Lanzirotti, A. (2018) Substitution and diffusion of Cr^{2+} and Cr^{3+} in synthetic forsterite and natural olivine at 1200–1500 °C and 1 bar. *Geochimica et Cosmochimica Acta*, 220, 407–428.

Kahl, M., Chakraborty, S., Costa, F., and Pompilio, M. (2011) Dynamic plumbing system beneath volcanoes revealed by kinetic modeling, and the connection to monitoring data: An example from Mt. Etna. *Earth and Planetary Science Letters*, 308, 11–22.

Kahl, M., Chakraborty, S., Costa, F., Pompilio, M., Liuzzo, M., and Viccaro, M. (2013) Compositionally zoned crystals and real-time degassing data reveal changes in magma transfer dynamics during the 2006 summit eruptive episodes of Mt. Etna. *Bulletin of Volcanology*, 75, 1–14.

Kahl, M., Chakraborty, S., Pompilio, M., and Costa, F. (2015) Constraints on the nature and evolution of the magma plumbing system of Mt. Etna Volcano (1991–2008) from a combined thermodynamic and kinetic modelling of the compositional record of minerals. *Journal of Petrology*, 56, 2025–2068.

Lazarov, M., and Horn, I. (2015) Matrix and energy effects during in-situ determination of Cu isotope ratios by ultraviolet-femtosecond laser ablation multicollector inductively coupled plasma mass spectrometry. *Spectrochimica Acta Part B: Atomic Spectroscopy*, 111, 64–73.

Lizarralde, D., Holbrook, W.S., Van Avendonk, H.J., Mora Fernandez, M., Alvarado, G.E., and Harder, S.H. (2010) Crustal structure along the active Costa Rican volcanic arc. In AGU Fall Meeting Abstracts, p. T13A–2176.

Longpré, M.-A., Klügel, A., Diehl, A., and Stix, J. (2014) Mixing in mantle magma reservoirs prior to and during the 2011–2012 eruption at El Hierro, Canary Islands. *Geology*, 42, 315–318.

Maaløe, S. (2011) Olivine phenocryst growth in Hawaiian tholeiites: Evidence for supercooling. *Journal of Petrology*, 52, 1579–1589.

Mallmann, G., O'Neill, H.St.C., and Klemme, S. (2009) Heterogeneous distribution of phosphorus in olivine from otherwise well-equilibrated spinel peridotite xenoliths and its implications for the mantle geochemistry of lithium. *Contributions to Mineralogy and Petrology*, 158, 485–504.

Milman-Barris, M.S., Beckett, J.R., Baker, M.B., Hofmann, A.E., Morgan, Z., Crowley, M.R., Vielzeuf, D., and Stolper, E. (2008) Zoning of phosphorus in igneous olivine. *Contributions to Mineralogy and Petrology*, 155, 739–765.

Oeser, M., Weyer, S., Horn, I., and Schuth, S. (2014) High-precision Fe and Mg isotope ratios of silicate reference glasses determined in situ by femtosecond LA-MC-ICP-MS and by solution nebulisation MC-ICP-MS. *Geostandards and Geoanalytical Research*, 38, 311–328.

Oeser, M., Dohmen, R., Horn, I., Schuth, S., and Weyer, S. (2015) Processes and time scales of magmatic evolution as revealed by Fe-Mg chemical and isotopic zoning in natural olivines. *Geochimica et Cosmochimica Acta*, 154, 130–150.

Otamendi, J.E., Tiepolo, M., Walker, B.A., Cristofolini, E.A., and Tibaldi, A.M. (2016) Trace elements in minerals from mafic and ultramafic cumulates of the central Sierra de Valle Fértil, Famatinian arc, Argentina. *Lithos*, 240–243, 355–370.

Papike, J.J., Karner, J.M., and Shearer, C.K. (2005) Comparative planetary mineralogy: Valence state partitioning of Cr, Fe, Ti, and V among crystallographic sites in olivine, pyroxene, and spinel from planetary basalts. *American Mineralogist*, 90, 277–290.

Qian, Q., O'Neill, H.St.C., and Hermann, J. (2010) Comparative diffusion coefficients of major and trace elements in olivine at ~950 °C from a xenocryst included in dioritic magma. *Geology*, 38, 331–334.

Rae, A.S.P., Edmonds, M., MacLennan, J., Morgan, D., Houghton, B., Hartley, M.E., and Sides, I. (2016) Time scales of magma transport and mixing at Kilauea Volcano, Hawai'i. *Geology*, 44, 463–466.

Richter, F.M., Liang, Y., and Davis, A.M. (1999) Isotope fractionation by diffusion in molten oxides. *Geochimica et Cosmochimica Acta*, 63, 2853–2861.

Richter, F.M., Davis, A.M., DePaolo, D.J., and Watson, E.B. (2003) Isotope fractionation by chemical diffusion between molten basalt and rhyolite. *Geochimica et Cosmochimica Acta*, 67, 3905–3923.

Richter, F., Chaussidon, M., Mendybaev, R., and Kite, E. (2016) Reassessing the cooling rate and geologic setting of Martian meteorites MIL 03346 and NWA 817. *Geochimica et Cosmochimica Acta*, 182, 1–23.

Rubin, A.M. (1995) Propagation of magma-filled cracks. *Annual Review of Earth and Planetary Sciences*, 23, 287–336.

Ruprecht, P., and Plank, T. (2013) Feeding andesitic eruptions with a high-speed connection from the mantle. *Nature*, 500, 68–72.

Ruprecht, P., Bergantz, G.W., and Dufek, J. (2008) Modeling of gas-driven magmatic overturn: Tracking of phenocryst dispersal and gathering during magma mixing. *Geochemistry, Geophysics, Geosystems*, 9, 1–20.

Schleicher, J.M., and Bergantz, G.W. (2017) The mechanics and temporal evolution of an open-system magmatic intrusion into a crystal-rich magma. *Journal of Petrology*, 58, 1059–1072.

Schwab, R.G., and Küstner, D. (1981) The equilibrium fugacities of important oxygen buffers in technology and petrology. *Neues Jahrbuch für Mineralogie Abhandlungen*, 140, 111–142.

Shea, T., Lynn, K.J., and Garcia, M.O. (2015) Cracking the olivine zoning code: Distinguishing between crystal growth and diffusion. *Geology*, 43, 935–938.

Sio, C.K.I., and Dauphas, N. (2017) Thermal and crystallization histories of magmatic bodies by Monte Carlo inversion of Mg-Fe isotopic profiles in olivine. *Geology*, 44, G38056.1.

Sio, C.K.I., Dauphas, N., Teng, F.-Z., Chaussidon, M., Helz, R.T., and Roskosz, M. (2013) Discerning crystal growth from diffusion profiles in zoned olivine by *in situ* Mg-Fe isotopic analyses. *Geochimica et Cosmochimica Acta*, 123, 302–321.

Spandler, C., and O'Neill, H.St.C. (2010) Diffusion and partition coefficients of minor and trace elements in San Carlos olivine at 1,300°C with some geochemical implications. *Contributions to Mineralogy and Petrology*, 159, 791–818.

Spandler, C., O'Neill, H.St.C., and Kamenetsky, V.S. (2007) Survival times of anomalous melt inclusions from element diffusion in olivine and chromite. *Nature*, 447, 303–306.

Teng, F.-Z., Dauphas, N., Helz, R.T., Gao, S., and Huang, S. (2011) Diffusion-driven magnesium and iron isotope fractionation in Hawaiian olivine. *Earth and Planetary Science Letters*, 308, 317–324.

Tollan, P.M.E., O'Neill, H.St.C., Hermann, J., Benedictus, A., and Arculus, R.J. (2015) Frozen melt-rock reaction in a peridotite xenolith from sub-arc mantle recorded by diffusion of trace elements and water in olivine. *Earth and Planetary Science Letters*, 422, 169–181.

Van Orman, J.A., and Krawczynski, M.J. (2015) Theoretical constraints on the isotope effect for diffusion in minerals. *Geochimica et Cosmochimica Acta*, 164, 365–381.

Wang, Z., Hiraga, T., and Kohlstedt, D.L. (2004) Effect of H^+ on Fe-Mg interdiffusion in olivine, $(\text{Fe},\text{Mg})_2\text{SiO}_4$. *Applied Physics Letters*, 85, 209–211.

Watson, E.B., Cherniak, D.J., and Holycross, M.E. (2015) Diffusion of phosphorus in olivine and molten basalt. *American Mineralogist*, 100, 2053–2065.

White, R.W. (1966) Ultramafic inclusions in basaltic rocks from Hawaii. *Contributions to Mineralogy and Petrology*, 12, 245–314.

Zhukova, I., O'Neill, H.St.C., Campbell, I.H., and Kilburn, M.R. (2014) The effect of silica activity on the diffusion of Ni and Co in olivine. *Contributions to Mineralogy and Petrology*, 168, 1029.

Zhukova, I., O'Neill, H., and Campbell, I.H. (2017) A subsidiary fast-diffusing substitution mechanism of Al in forsterite investigated using diffusion experiments under controlled thermodynamic conditions. *Contributions to Mineralogy and Petrology*, 172, 1–12.

MANUSCRIPT RECEIVED JULY 26, 2017

MANUSCRIPT ACCEPTED DECEMBER 18, 2017

MANUSCRIPT HANDLED BY RENAT R. ALMEEV

Endnote:

¹Deposit item AM-18-46258, Supplemental Material. Deposit items are free to all readers and found on the MSA web site, via the specific issue's Table of Contents (go to http://www.minsocam.org/MSA/AmMin/TOC/2018/Apr2018_data/Apr2018_data.html).